DIRECT NANO-PATTERNING WITH NANO-OPTIC DEVICES

A Thesis

by

VIJAY MEENASHI SUNDARAM

Submitted to the Office of Graduate Studies of
Texas A&M University
in partial fulfillment of the requirements for the degree of

MASTER OF SCIENCE

May 2010

Major Subject: Mechanical Engineering

Direct Nano-patterning with Nano-optic Devices

DIRECT NANO-PATTERNING WITH NANO-OPTIC DEVICES

A Thesis

by

VIJAY MEENASHI SUNDARAM

Submitted to the Office of Graduate Studies of
Texas A&M University
in partial fulfillment of the requirements for the degree of

MASTER OF SCIENCE

Approved by:

Co-Chairs of Committee,	Sy-Bor Wen
	Chii-Der Suh
Committee Members,	Chin Su Bing
Head of Department,	Dennis O'Neal

May 2010

Major Subject: Mechanical Engineering

ABSTRACT

Direct Nano-patterning with Nano-optic Devices. (May 2010)

Vijay Meenashi Sundaram, B.Tech., National Institute of Technology, Trichy

Co-Chairs of Advisory Committee: Dr. Sy-Bor Wen
Dr. Chii-Der Suh

In this study nano-patterning was carried out using two different nano-optic devices namely – the NSOM and Fresnel zone plate.

In the first study, NSOM was used to generate nano-patterns on selected semiconducting (Si & Ge) and metallic (Cr, Cu and Ag) targets under different laser pulse durations, laser energies and number of laser pulses. Based on the experimental results, femtosecond laser pulses, provided lower pattern generation thresholds on targets but higher damage thresholds to the NSOM probes at the wavelength (~400-410 nm) studied, compared with nanosecond laser pulses. Three different mechanisms were identified as the dominant processes for pattern generation under different conditions, namely nano-scale laser ablation, nano-scale thermal oxidation and nano-scale melting/recrystallization of the targets. Furthermore, the resulting nano-patterns also showed a significant dependence on the optical properties (i.e., absorption coefficient and surface reflectivity) of the target material. By comparing the obtained experimental results, it was concluded that the optical energy transport from the NSOM probe to the target dominates the pattern generation when femtosecond laser is applied to the NSOM system. When nanosecond laser is applied, both the thermal and optical energy transported from the NSOM probe to the targets attribute to the obtained morphology of nano-patterns on different targets under the experimental conditions studied.

In the second study, a traditional Fresnel zone plate with a focus length of 3μm was fabricated with a novel lift-off process in e-beam lithography. The fabrication process

involved, using a HSQ/PMMA bi-layer in a negative tone lift-off process with a layer of conducting polyaniline for charge dissipation. HSQ was used as the high resolution negative resist for e-beam patterning and the PMMA under-layer was used to enable a HSQ lift-off process. The fabricated Fresnel zone plate was used to generate nano-patterns on a UV sensitive photoresist using nanosecond laser light with $\lambda \sim 409nm$. The smallest pattern sizes generated was close to the diffraction limit. Nano-pattern sizes generated on the photoresist were comparable with a numerically calculated intensity distribution at the focus spot of the designed Fresnel zone plate obtained from Scalar Diffraction Theory.

DEDICATION

To my parents

ACKNOWLEDGEMENTS

TABLE OF CONTENTS

LIST OF FIGURES

Page

LIST OF TABLES

1. INTRODUCTION

1.1 Laser

Light Amplification by Stimulated Emission of Radiation (Laser) is a class of devices that can generate coherent radiation at frequencies in the infrared, visible or ultraviolet regions of the electromagnetic spectrum. The emitted laser light can be a spatially coherent, narrow, low divergence beam that can be directed with active and passive optical devices.

The basic laser structure consists of an active medium consisting of a collection of atoms, molecules or ions, a pumping source that pumps energy into the medium to excite these atoms into higher energy levels, and an optical resonator consisting of two highly reflecting components that bounce the laser beam back and forth repeatedly through a lasing medium. The pump source could be a flash-lamp, a gas discharge, or an electrical current source. Depending on the nature of the active medium and the amplification process, lasers can be classified as gas lasers, chemical lasers, excimer lasers or solid state lasers. The output of laser can be continuous constant amplitude light (known as continuous wave lasers) or pulsed. Continuous wave lasers have been used in a variety of applications like laser printing, bar-code reading, microscopy, flow diagnostics etc. However for applications that require controlled deposition of intense laser energy in a very short time, pulsed lasers are being used. The pulsed operation is achieved using techniques like q-switching, mode locking or gain switching and leads to much higher peak powers.

This thesis follows the style of Journal of Applied Physics.

1.2   Laser Nano-Patterning

Laser ablation is the phenomenon of material removal induced by intense pulsed laser light on the surface of a material [1,2]. Laser ablation can be due to heating, melting and vaporization of the target materials along with Coulomb explosion when high enough laser fluence is applied. The size and shape of the craters induced by pulsed laser ablation depend on the optical properties of the target materials. The region in the material which is thermally modified due to the influence of the laser is commonly named as the heat affected zone (HAZ) [1]. Laser ablation is applied commonly in (a) pulsed laser deposition, (b) direct laser machining, and (c) laser cleaning. Recently, laser ablation has also been used for the generation of nano-particles by controlling the condensation process of laser induced plasma. Laser spectroscopy analyses, which utilizes the laser induced plasma from laser ablation to determine the chemical composition of the material, is an important application of laser ablation [3]. Laser ablation also finds its applications in biology where intense laser light is used to kill tissues and cells [4].

With the recent advances in nanotechnology, there arise needs to extend the science and technology of laser processing including laser ablation to the nano-scale. With the much lower laser operation cost and little influence by background gas, nano-fabrication through laser has become a potential candidate for next generation tools for nano-fabrication [5]. Although there are other available techniques like electron beam, ion beam and x-rays for nano-scale processing, the excessive costs, along with the requirement for vacuum conditions limit the application of these techniques compared with nano-scale processing with laser ablation.

Nano-patterning on a material with a laser requires confinement of the laser light to a nanometer spot. Even with a perfectly designed optical lens that is free from all forms of aberrations, the smallest focus possible is limited by the theoretical diffraction limit (<~

$\lambda/2$ limit). One way to reduce the spot size, while still using traditional optical devices, is through using shorter wavelengths such as deep UV (DUV) or extreme UV (EUV) light. However, the limited availability of laser optics in this short wavelength along with the possible strong absorption in the atmosphere, limits the application of short wavelength in many academic and industrial applications.

Nano-optics is a new group of optical elements which can surpass the $<\sim \lambda/2$ limit (super-resolution). In nano-optics, mechanisms such as evanescent waves and light interferences, which do not suffer from far field diffraction limit in comparison with traditional optical devices (e.g., lenses and optical fibers), are used to focus light [6]. Two particularly important classes of devices have a tremendous potential for sub-diffraction limit focusing, namely, near field scanning optical microscope (NSOM) and plasmonic optical devices. In NSOM, evanescent wave is utilized to better focus the incident laser energy while in plasmonic optical devices the surface plasmon polariton (SPP) on metallic surfaces are utilized to better focus the light energy. The purpose of this master's study is to examine the possibility of both devices in nanoscale direct patterning or even nanoscale direct laser ablation.

1.3   Near Field Scanning Optical Microscope (NSOM)

The apertured Near Field Scanning Optical Microscope (NSOM) is a commercialized nano-optic device that achieves sub-diffraction limit resolution by confining light to the near-field [7,8]. The apertured NSOM probe consists of a tapered metal-coated optical fiber with a sub-diffraction limit aperture that emits highly confined light for sub-diffraction limit imaging and detection. Nanoscale Raman scattering [9,10], nanoscale fluorescence along with nano-lithography [11] have been achieved through a combination of near field scanning optical microscope (NSOM) with coherent light sources.

Based on the previous success of nano-scale detection with NSOM under low laser

fluence, a possible application lies in using the NSOM for near-field nano-scale fabrication through increasing the incident light intensity. Recently nano-meter scale direct fabrication has been achieved by coupling pulsed laser light into an NSOM. Nanoscale direct fabrication (nanoscale laser ablation) through a combination of NSOM and a pulsed laser source, compared with other techniques for such as focused ion beam and focused electron beam, can be performed in an environment with background gas. Therefore, nanoscale NSOM laser ablation has its applications in nano-machining, nano-optical surgery, and nano-chemical analysis when a background gas environment is required.

It is demonstrated in a previous experimental and theoretical study that apertured NSOM probe, under high laser fluence, can be used to generate nano-craters on a pure silicon wafer when a pulsed femtosecond laser is utilized as the light source [12,13]. However, the same prediction may not be valid when femtosecond laser is replaced with a nanosecond laser. Also, the dominant mechanisms for pattern generation identified in previous studies may not still be valid when the optical, material and background gas conditions are changed. To better understand the characteristics and the mechanisms of nano-patterning with a combination of pulsed laser and NSOM systems, controlled experiments with same experimental setup are required.

In this thesis, controlled experiments were conducted under different experimental conditions covering different optical pulse width, different laser pulse energy and targets with different material properties. From the controlled experiments, the contribution of each physical parameter on the nano-patterning process is revealed. Furthermore, through a comparison of the resulting pattern size, shape and chemical compositions under the different experimental conditions studied, potential mechanisms responsible for nano-patterning with a combination of NSOM system and pulsed laser sources were identified and categorized as a function of physical parameters tested. These observations are important for future nano-science applications with NSOM probes under high intense laser energy.

1.4   Micro-Zone Plate (Preliminary Study for SPP Zone Plate)

Diffractive optics is a class of lenses that use diffraction to focus light. Unlike the traditional refractive optic lenses, diffractive optics can operate in visible, UV, DUV, EUV and x-ray wavelengths. A zone plate is one of the diffractive optical devices that constructs diffraction pattern through alternative transparent and opaque zones. Zone plates are extensively used for focusing of the shorter wavelengths especially x-rays where refractive optic lenses are too expensive or not available.

The simplest form of a zone plate consists of a set of concentric rings with alternate transparent and opaque zones (these zones are opaque to the incident radiation). A parallel beam of light when incident on one side of the zone plate can be brought to a focus on the other side, similar to a traditional refractive optic convex lens. The basic principle of operation of a zone plate can be understood from Huygens Principle. Huygens principle states that every point on a wave-front is assumed to be the center of a system of secondary wavelets, and the new wave-front is the common tangent of these waves. Thus, by considering the mutual interference that occurs between these secondary waves, diffraction effects can be demonstrated. This forms the basis of the Fresnel zones that arise due to diffraction from an aperture. The zone plate structure is an extension of these Fresnel zones. The location and width of each of these concentric zones is designed to ensure that the first order diffracted radiation from any transparent zone crosses the axis of the zone plate at the same focus point. A number of techniques are available to improve both the focusing and the energy transport efficiency of Fresnel zone plates. The common modifications includes the phase zone plate and fractal zone plate [14].

Nano-lithography using Fresnel zone plates have been performed with x-rays [15]. Subsequently, an array of phase zone plates was used to perform nano-lithography in the deep UV regime [16]. Immersion zone plate array lithography (ZPAL) has been developed

to further improve the resolution by increasing the numerical aperture of the zone plate [17]. These techniques for ZPAL use zone plates with focal lengths of ~50 micron and require a large number of zones to achieve high resolution. All these methods are, however, still diffraction limited.

One possible methodology for improving focusing of the zone plate comes from the evidence of enhanced light transmission, much greater than that predicted by Bethe's theory, occurring at sub-wavelength diameter holes/slits on metal films [18]. Garcia Videl and coworkers showed that, by properly arrange the sub-diffraction limits slits, light can be focused to a very narrow string [19]. These recent works on SPP enhanced optical transmission through sub-wavelength slits allows much narrower slits (or zones) to be applied in the design of micro zone plates (MZP or PMZP-plasmonic micro zone plates). Various MZPs utilizing SPP to enhance optical transmission and provides a focal lengths ranging from 2-5 microns have been proposed and demonstrated in the recent few years [20]. Furthermore, a number of design modifications by several groups have theoretically predicted sub-diffraction focusing when the zone width of the zone plates is smaller than the diffraction limit [21]. Compared with NSOM, sub-diffraction limit focusing with Micro zone plates (with SPP enhanced sub-diffraction limit zones) allow working distances in the micrometers rather than nanometers like traditional NSOM (~10-20nm). However a major challenge lies in fabrication of micro zone plates (most of which have very fine features) and design of an experimental setup where it can be tested. Although current lithographic techniques like e-beam lithography can achieve a resolution of 20-30nm, issues like substrate charging and proximity effect which occur during fabrication on insulating substrates make micro zone plate fabrication very challenging.

The second portion of the thesis focuses on constructing and examining traditional Fresnel micro zone plates fabricated with a novel lift-off process developed during the master's study. This novel lift-off process is composed with electron beam lithography

using a conducting polymer, and multiple photoresist layers. The light focusing capability of the fabricated zone plate was tested by pattern generation on photoresist. The zone plate consisted of concentric ring apertures in a silver thin film on a fused-silica substrate. Note that even though sub-diffraction limit zone plates with SPP enhanced sub-diffraction zones is still under study in our group, the novel fabrication procedure employed in this study provides a standard route for future fabrication of plasmonic Fresnel zone plates.

2. NANO-PATTERNING WITH NSOM – THEORY

2.1 Far-field Focusing

According to Abbe's theory of far-field image formation, the resolving power of an optical component is limited by the spreading out of each image point due to diffraction. The theoretical limit of far-field focusing and image formation can be derived in the following manner [22].

Consider a monochromatic plane wave travelling along the x direction, incident on a screen with an arbitrary aperture (Figure 1). At some point P at a distance R from the aperture (in the far-field), the field distribution can be determined from the Huygens-Fresnel Principle. Considering each elemental area (denoted by dS at location (y, z) on the aperture) as a point emitter, the total disturbance arriving at point P (denoted by (Y, Z) on the screen) in the far-field is given by

$$E = \frac{E_A e^{i(\omega t - kR)}}{R} \iint\limits_{Aperture} e^{ik(Yy+Zz)/R} dS \qquad (2.1)$$

where E_A is the source strength per unit area, which is assumed to be a constant. For a circular aperture of radius a, the expression can be written in spherical coordinates, with (ρ, ϕ) denoting the aperture plane and (q, Φ) denoting the image plane, as

$$E = \frac{E_A e^{i(\omega t - kR)}}{R} \int\limits_{\rho=0}^{a} \int\limits_{\phi=0}^{2\pi} e^{i(kq/R)\cos(\phi-\Phi)} \rho d\rho d\phi \qquad (2.2)$$

This expression can be rewritten in terms of the zero-order Bessel function as

$$E(t) = \frac{E_A e^{i(\omega t - kR)}}{R} 2\pi \int\limits_{0}^{a} J_0(k\rho q/R)\rho d\rho = \frac{E_A e^{i(\omega t - kR)}}{R} 2\pi a^2 (R/kaq) J_1(kaq/R) \quad (2.3)$$

where J_1 denotes the first order Bessel Function. The irradiation at point P is given by $<(\text{Re}\,E)^2>$ or $\frac{1}{2}EE^*$ that is

$$I = \frac{2\mathrm{E}_A^2 A^2}{R^2} \left[\frac{J_1(kaq/R)}{kaq/R} \right]^2, \tag{2.4}$$

where A denotes the area of the aperture and q denotes the radial distance on the image plane. Therefore to determine the irradiation at the center of the image plane we have to have $q=0$. A plot of this function shows an axially symmetric distribution, with a high irradiation central spot (know as Airy's disk) surrounded by alternating bright and dark rings (known as side lobes) of decreasing intensity from $q=0$. The dark rings correspond to the zeros of the first order Bessel function. The radius of the Airy's disk can be obtained from the first zero of the Bessel function $J_1(x)=0$ when $x=3.832$ that is,

$$\frac{kaq_1}{R} = 3.83 \Rightarrow q_1 = 1.22\frac{R\lambda}{2a} \tag{2.5}$$

If the circular aperture is replaced by a lens, then R denotes the focal length f, and $2a$, denotes the lens diameter D, so

$$q_1 = 1.22\frac{f\lambda}{D} \tag{2.6}$$
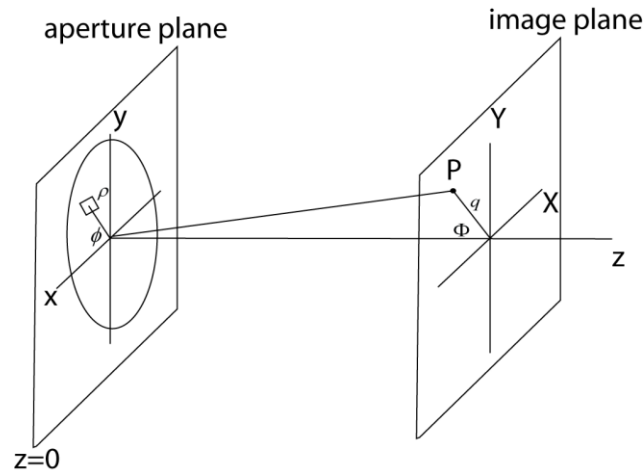
Figure 1: Far-field diffraction showing the aperture and image plane

This denotes the smallest possible spot that can be produced by a traditional lens in the far field. This limit also applies to detection of an object in the far field of a lens. The

object can be considered to consist of a number of point sources that scatter light. The scattered light is captured by the lens system which forms an image of the object, consisting of a distribution of Airy disks. For a lens system that is completely free from aberrations, two points on the object can be resolved only if their Airy disks don't overlap (Rayleigh Criterion). Hence diffraction puts an ultimate limit on image quality in far-field microscopy.

2.2   Light Propagation Though NSOM Probe

Apertured NSOM probes consist of a tapered dielectric coated with a metal thin film coating. The metal coating prevents the fields from leaking through the sides of the probe. The light propagation through the NSOM probe can be understood by considering it to be a tapered hollow metal waveguide filled with a dielectric material [6]. The modes existing in a cylindrical waveguide depend on the diameter of the dielectric core of the waveguide. For larger diameters there exist a large number of guided modes. As the diameter decreases towards the apex of the NSOM probe these modes run into cut off i.e. the propagation constant of the mode becomes purely imaginary and the mode becomes evanescent. After a certain diameter of the tapered dielectric all the guided modes become evanescent and decay exponentially towards the apex of the probe. If we consider the incident light into the NSOM fiber to contain all the possible modes the final mode to reach cut-off will be the HE_{11} mode which is preceded by the TE_{01} and TM_{01}. This mode cut-off is the reason for low-light throughput from apertured NSOM probes. However the final light spot emitted into the near field of the probe is highly confined and the spot size is a function of only the aperture size (Figure 2).

 This mode cut off behavior is used to effectively design the NSOM probe. The larger the taper angle, the better will be the light throughput, since the final mode cut-off diameter lies closer to the tip apex. When a mode becomes evanescent, the energy carried by it exponentially decays towards the apex and is partly dissipated into the

metal coating. This causes significant heating of the metal coating and puts a limit on the maximum power that can be transmitted through an NSOM probe.
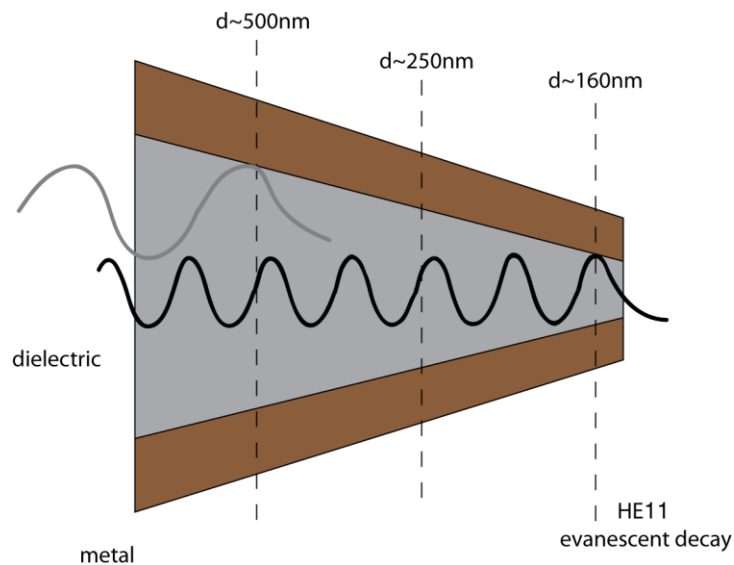
Figure 2: Schematic showing mode decay in an NSOM probe

The cut-off of a guided mode propagating through the NSOM probe into an evanescent wave that decays exponentially towards the tip apex can be explained in the following manner [23].

Consider a cylindrical dielectric waveguide of radius a, with a permittivity of ε_1 immersed in an infinite medium of permittivity ε_2 such that $\varepsilon_1 > \varepsilon_2$. (see Figure 3)
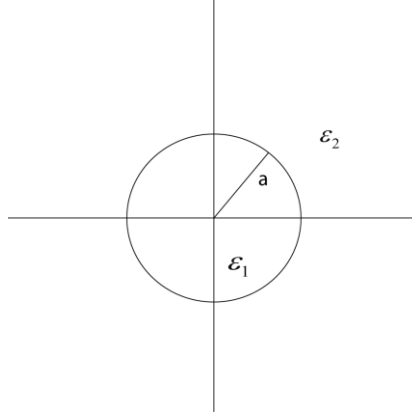
Figure 3: Schematic of waveguide considered for analysis of modes

If we consider an electromagnetic wave of angular frequency ω propagating down the waveguide along the z direction, the electric and magnetic fields can be written as

$$E(r,\theta,z,t) = E(r,\theta)e^{i(kz-\omega t)},$$
$$H(r,\theta,z,t) = H(r,\theta)e^{i(kz-\omega t)}$$
(2.7)

Based on this assumption, the wave equation can be modified to represent only E_z and H_z. The remaining two components of the E and H field (namely E_r, E_θ and H_r, H_θ) can be obtained from E_z and H_z using the source free Maxwell's Equations. The solution to the wave equation in cylindrical coordinates

$$\left[\frac{1}{r}\left(\frac{\partial}{\partial r}r\frac{\partial}{\partial r}+\frac{\partial}{\partial \theta}r\frac{\partial}{\partial \theta}\right)+p^2\right]\begin{bmatrix}E_z\\H_z\end{bmatrix}=0,$$
(2.8)

where,

$$p^2 = \omega^2\mu_0\varepsilon - k^2$$
(2.9)

is given by the Bessel function where n is an integer,

$$E_z^{(1)}(r,\theta) = \sum_{n=0}^{\infty} A_n J_n(p_1 r)e^{in\theta},$$
$$H_z^{(1)}(r,\theta) = \sum_{n=0}^{\infty} B_n J_n(p_1 r)e^{in\theta}$$
(2.10)

Here (1) denotes the medium 1 inside the waveguide and

$$p_1^2 = k_1^2 - k^2,$$
$$k_1^2 = \omega^2\mu_0\varepsilon_1$$
(2.11)

Using the Maxwell's equations the remaining components of the electric and magnetic field inside the waveguide can be found to be

$$E_r^{(1)}(r,\theta) = \frac{1}{p_1^2} \sum_{n=0}^{\infty} \left[-ikp_1 A_n J_n'(p_1 r) + \frac{\omega\mu_0 n}{r} B_n J_n(p_1 r) \right] e^{jn\theta},$$

$$E_\theta^{(1)}(r,\theta) = \frac{1}{p_1^2} \sum_{n=0}^{\infty} \left[\frac{kn}{r} A_n J_n(p_1 r) + j\omega\mu_0 p_1 B_n J_n'(p_1 r) \right] e^{jn\theta},$$

$$H_r^{(1)}(r,\theta) = \frac{1}{p_1^2} \sum_{n=0}^{\infty} \left[-\frac{\omega\varepsilon_1 n}{r} A_n J_n(p_1 r) - jkp_1 B_n J_n'(p_1 r) \right] e^{jn\theta},$$

$$H_\theta^{(1)}(r,\theta) = \frac{1}{p_1^2} \sum_{n=0}^{\infty} \left[-j\omega\varepsilon_1 p_1 A_n J_n'(p_1 r) + \frac{kn}{r} B_n J_n(p_1 r) \right] e^{jn\theta},$$

$$(2.12)$$

In the region outside the waveguide, denoted by medium 2, the field is described by the modified Bessel function which decays to 0,

$$E_z^{(2)}(r,\theta) = \sum_{n=0}^{\infty} C_n K_n(q_2 r) e^{in\theta},$$

$$H_z^{(2)}(r,\theta) = \sum_{n=0}^{\infty} D_n K_n(q_2 r) e^{in\theta}$$

$$(2.13)$$

Here (2) denotes the medium 2 outside the waveguide and

$$q_2^2 = k^2 - k_2^2,$$

$$k_2^2 = \omega^2 \mu_0 \varepsilon_2$$

$$(2.14)$$

In a similar manner as (2.12), the transverse components of the electric and magnetic fields outside the waveguide can be obtained from the Maxwell's equation giving,

$$E_r^{(2)}(r,\theta) = -\frac{1}{q_2^2} \sum_{n=0}^{\infty} \left[-ikq_2 C_n K_n'(q_2 r) + \frac{\omega\mu_0 n}{r} D_n K_n(q_2 r) \right] e^{jn\theta},$$

$$E_\theta^{(2)}(r,\theta) = -\frac{1}{q_2^2} \sum_{n=0}^{\infty} \left[\frac{kn}{r} C_n K_n(q_2 r) + j\omega\mu_0 p_1 D_n K_n'(q_2 r) \right] e^{jn\theta},$$

$$H_r^{(2)}(r,\theta) = -\frac{1}{q_2^2} \sum_{n=0}^{\infty} \left[-\frac{\omega\varepsilon_1 n}{r} C_n K_n(q_2 r) - jkp_1 D_n K_n'(q_2 r) \right] e^{jn\theta},$$

$$H_\theta^{(2)}(r,\theta) = -\frac{1}{q_2^2} \sum_{n=0}^{\infty} \left[-j\omega\varepsilon_1 p_1 C_n K_n'(q_2 r) + \frac{kn}{r} D_n K_n(q_2 r) \right] e^{jn\theta},$$

$$(2.15)$$

In order to evaluate the constants A_n, B_n, C_n and D_n, we consider the boundary conditions, i.e. at the boundary surface $r=a$, the tangential fields must be continuous.

This also gives the dispersion relation for an electromagnetic wave travelling in a cylindrical waveguide. The boundary conditions are given by

$$
\begin{aligned}
E_z^{(1)}(a,\theta) &= E_z^{(2)}(a,\theta), \\
H_z^{(1)}(a,\theta) &= H_z^{(2)}(a,\theta), \\
E_\theta^{(1)}(a,\theta) &= E_\theta^{(2)}(a,\theta), \\
H_\theta^{(1)}(a,\theta) &= H_\theta^{(2)}(a,\theta),
\end{aligned}
\tag{2.16}
$$

Substituting for these expressions from (2.15), (2.13), (2.12) and (2.10) we get 4 independent equations to evaluate the 4 unknowns. The equations can be written in the form

$$
[M]\begin{bmatrix} A_n \\ B_n \\ C_n \\ D_n \end{bmatrix} = 0
\tag{2.17}
$$

In order to get non-trivial solutions for A_n, B_n, C_n and D_n, the determinant of M must be set to zero. This gives the dispersion relation for the electromagnetic wave propagating through a dielectric waveguide i.e.

$$
\left[\frac{J_n'(p_1 a)}{p_1 J_n(p_1 a)} + \frac{K_n'(q_2 a)}{q_2 K_n(q_2 a)}\right]\left[\frac{k_1^2 J_n'(p_1 a)}{p_1 J_n(p_1 a)} + \frac{k_2^2 K_n'(q_2 a)}{q_2 K_n(q_2 a)}\right] = \left(\frac{kn}{a}\right)^2\left(\frac{1}{p_1^2} + \frac{1}{q_2^2}\right)^2
\tag{2.18}
$$

From this equation, it is possible to get the propagation constant k, which will satisfy the equation. Also, since n, is an integer there exists a distinct dispersion relation for each value of n. For the circular symmetric case, $n=0$, so the RHS of equation (2.18) is 0, i.e. the boundary conditions are satisfied by TE and pure TM waves (based on zero order Bessel function)

TE$_{0m}$ Modes:

$$
\frac{J_0'(p_1 a)}{p_1 J_0(p_1 a)} + \frac{K_0'(q_2 a)}{q_2 K_0(q_2 a)} = 0
\tag{2.19}
$$

TM$_{0m}$ Modes:

$$
\frac{k_1^2 J_0'(p_1 a)}{p_1 J_0(p_1 a)} + \frac{k_2^2 K_0'(q_2 a)}{q_2 K_0(q_2 a)} = 0
\tag{2.20}
$$

For the $n \neq 0$ case hybrid modes (HE) are needed to satisfy the boundary conditions.

A. Cut off Conditions

In order to have propagating real fields in the dielectric waveguide, the propagation constants must be real both inside and outside the waveguide,

$$p_1 > 0$$
$$q_2 > 0$$

(2.21)

Therefore from equations (2.11) and (2.14),

$$k_1 < k < k_2$$

At cutoff the modes no longer decay outside the dielectric. Therefore the field is no longer confined to the core. So, at cut-off, $q_2 = 0$. Therefore eliminating k from equations (2.11) and (2.14), the cut off frequency inside the waveguide is given by,

$$\omega_{cutoff} = \frac{p_1 c}{\sqrt{\varepsilon_1^2 - \varepsilon_2^2}}$$

(2.22)

In the above equation p_1 can be obtained from the dispersion relation (2.18), by setting $q_2a = 0$, i.e.

for the TE$_{0m}$ and TM$_{0m}$ modes

$$J_0(p_1 a) = 0,$$

(2.23)

and for the HE$_{1m}$ modes

$$J_1(p_1 a) = 0,$$

(2.24)

If we determine the cut-off frequency from these equations we find that only one mode, the HE$_{11}$ mode, has zero cut off frequency since the first root of (2.24) occurs at $p_1 a = 0$. The HE$_{11}$ mode is thus the most dominant mode. The second lowest cut-off frequency occurs for the TE$_{01}$ and the TM$_{01}$ modes. This is followed by the higher modes. For frequencies lower than the cut off frequencies, the propagation constant of the mode becomes imaginary and the corresponding mode decays along the length of the fiber.

3. NANO-PATTERNING WITH NSOM – EXPERIMENT

3.1 Experimental Setup

For nanosecond experiment, Nd-YAG laser with optical parametric oscillator (OPOTEK Vibrant 355 II) operating at 409 nm and a pulse duration ~4 ns was utilized as the light source. For femtosecond laser experiments, Ti:Sapphire femtosecond laser (Spectra Physics) operating at ~401 nm with ~10 nm spectral width and ~150 fs pulse duration was utilized. The triggering of both lasers was synchronized with the commercial NSOM system (Nanonics Inc.) through a delay generator (SRS DG535). Emitted light from both lasers were conducted to the entrance of NSOM probes through an optical fiber coupler (Thorlab Inc.). A camsplice was installed in the middle of the spliced NSOM optical fiber carrying laser energy from the optical fiber coupler to the NSOM tip (see Figure 4). The laser energy carried with the optical fiber was measured at the spliced point with a pJ sensitive energy meter (Coherent Inc.). All the NSOM probes (purchased from Nanonics Inc.) had an aperture diameter of ~200 nm with a thin gold coating (~100 nm) outside in order to confine light to a sub-diffraction limit region around the NSOM tip. During the experiments, a constant separation (~10nm) distance was maintained between the NSOM tip and the targets through a closed loop control of the commercial NSOM system.

Targets examined in this study were pure silicon wafers, pure germanium wafers, and chromium /copper/silver thin film coatings (~250-300 nm) on quartz plates. The thin film metal samples were prepared with thermal evaporation (BOC Edwards 307 Evaporator). The depositions were conducted at ~10^{-6} Torr with a deposition rate of 0.02-0.2nm/s to ensure smooth surfaces. The generated nano-patterns after each experiments were scanned with atomic force microscope (Veeco, tip diameter <2nm) in order to obtain the topography images. To determine the presence of SiO2 in the nano-patterns generated under different experimental conditions, Si samples after near field laser-material interactions were processed with buffered hydrogen fluoride solution

(BHF 7:1) for ten minutes and then scanned again with the AFM. Note that BHF selectively etches silicon dioxide (SiO_2) and silicon nitride (Si_3N_4) with an etching rate of ~100 nm/min for SiO_2 and only ~0.5-1 nm/min for Si_3N_4 [24].

To analyze the chemical composition of the nano-patterns generated on silicon using nanosecond laser, the experiment was conducted using air and argon as the background gases. The surface topography images were determined from NSOM scanning first and then a high resolution scanning with an atomic force microscope (Veeco AFM) before and after each experiment. Samples after the experiments were also (a) dipped in buffered hydrogen fluoride solution (BHF 7:1) for two minutes and then scanned again with an AFM, (b) examined with energy dispersive X-ray spectrometer (EDS) and X-ray photoelectron spectroscopy (XPS), (c) diced with focused ion beam and then studied with transmission electron microscopy (TEM).
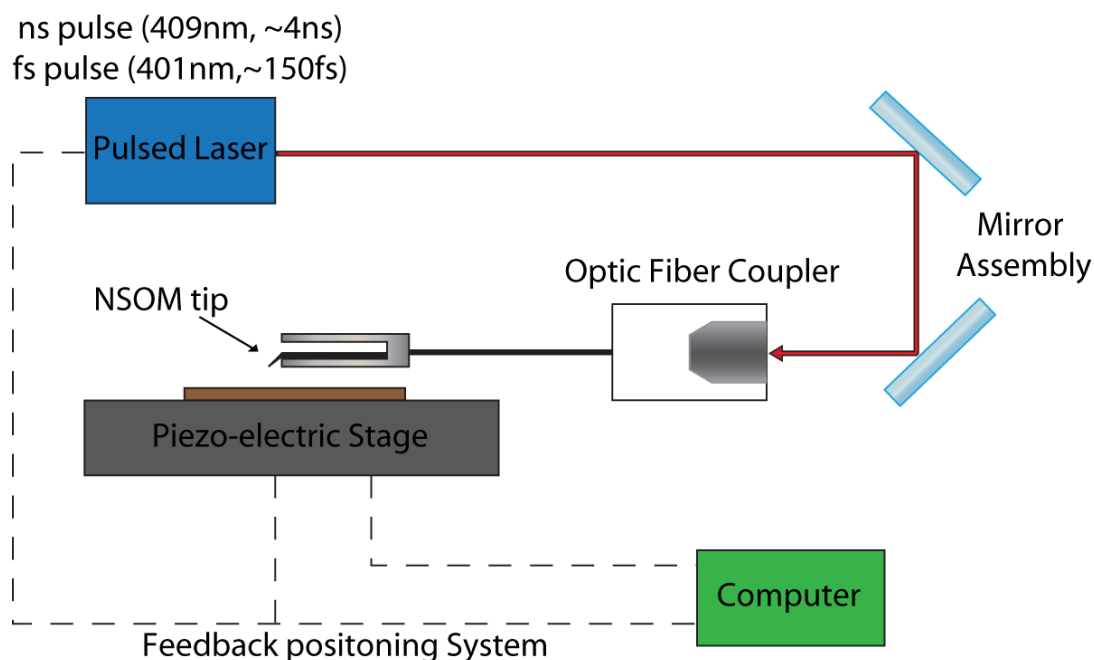
Figure 4: Schematic of experimental setup

3.2   Results and Discussion

The obtained experimental results with the above experimental setup under different (a) target materials (Si, Ge, Cr and Ag), (b) pulse durations (fs vs. ns), (c) laser energy, and (d) number of laser pulses are grouped and listed as follows:

1) Near field laser-material interaction with semi-conducting materials (Si & Ge)

Silicon and germanium were selected as the experimental targets considering both materials have similar thermal properties but significantly different optical absorption coefficient at λ~400-410 nm (Appendix A). Ge has much higher absorption coefficient than Si at λ~400-410 nm. Through comparing the experimental results from Si and Ge respectively, contribution of optical absorption coefficient in the near field laser-material interaction along with the associated mechanisms in nano-pattern generation is expected to be revealed. The results from Si and Ge with ns and fs laser pulses are listed as follows:

a)   For nanosecond laser pulses

Si: Nano-patterns were observed on intrinsic Si wafers when E > ~1.8 − 2.0 nJ after 300 pulses. The shape of the nano-pattern remained a protrusion for different number of laser pulses (i.e. 300 to 1200 pulses, Figure 5 and Table 1). The diameter of the nano-protrusions generated in air varied from 1200 nm to 1400 nm while the height of the protrusions increased from 6 nm to 18 nm (Table 2) after 300-1200 laser pulses.
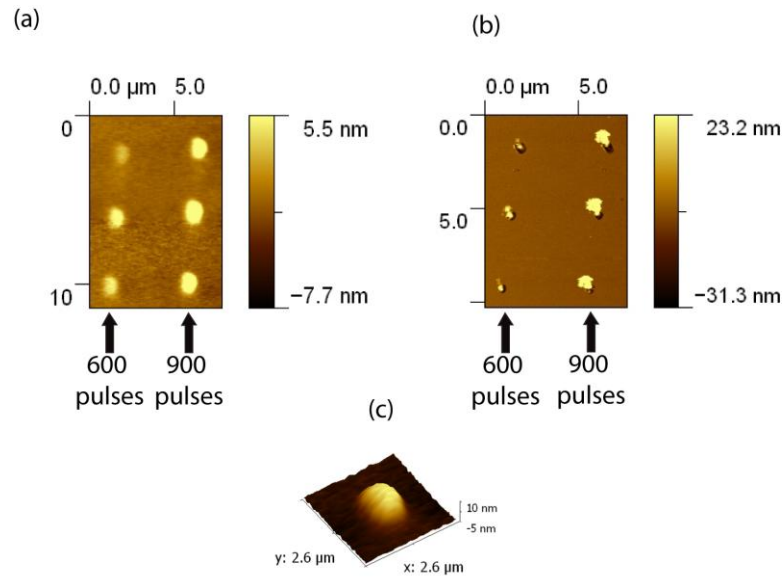
Figure 5: Nano-patterns generated on silicon using nanosecond laser (a) before etching with BHF (b) after etching with BHF (c) protrusion after 900 laser pulses

Ge: Nano-patterns were observed on intrinsic germanium wafers after 50 laser pulses when the input laser energy was >1.7 nJ, which is about 0.1-0.3 nJ lower than the damage threshold of Si wafers. Unlike the patterns generated on silicon, the nano-patterns generated on germanium were in crater format for all the number of laser pulses studied (Figure 6). The diameter of the nano-patterns increased from 700 nm to 900 nm after 900-1800 laser pulses (Table 1) while the depths of the protrusions increased from 15 nm to 25 nm after 900-1200 pulses (Table 2).
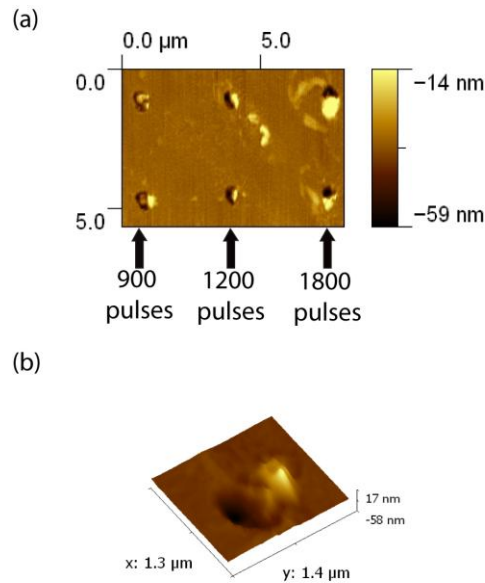
Figure 6: Nano-patterns generated on germanium using nanosecond laser (a) 2-D image after 900, 1200 and 1800 laser pulses (b) crater after 900 laser pulses

b) For femtosecond laser pulses

Si: Nano-patterns were observed on intrinsic Si wafers with femtosecond laser all the three laser energies studied (i.e., 1, 2 and 3 nJ). The shape of nano-patterns evolved from nano-craters (for single and few pulses) to nano-protrusions gradually when the number of laser pulses increased from 50 to 300 for all the three laser energies studies (see Figure 7). The diameter of the nano-patterns increased from 500 nm to 1000 nm (Table 1) while the depth of the protrusion increased from 8 nm to 50 nm at E ~2nJ (Table 2) after 50-600 laser pulses.
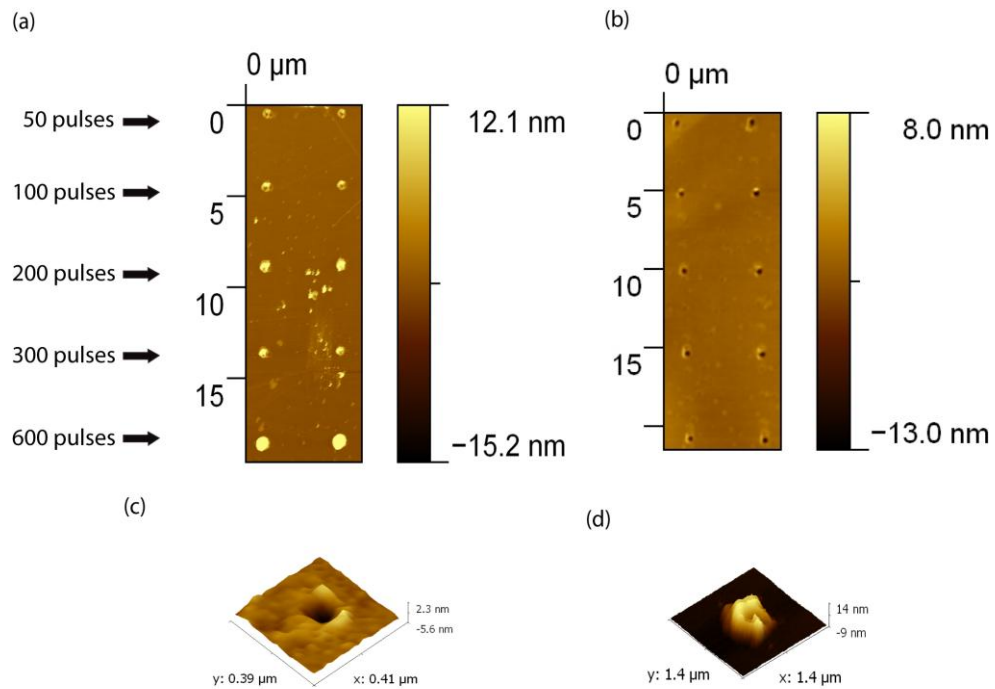
Figure 7: Nano-patterns generated on silicon using femtosecond laser (a) before etching with BHF (b) after etching with BHF (c) after single pulse (d) after 200 laser pulses

Ge: Nano-patterns were also observed on intrinsic germanium wafers with femtosecond laser, for all the three laser energies studied (i.e., 1, 2 and 3 nJ). Compared with the results on Si wafers, the resulting patterns on intrinsic germanium wafers were nano-craters for all laser energies and number of laser pulses studied (i.e., 1 to 600 pulses, Figure 8). The diameter of the nano-craters varied from 500 nm to 900 nm (Table 1) while the depth of the nano-craters increased from 15 nm to 55 nm (Table 2) after 50-600 laser pulses.
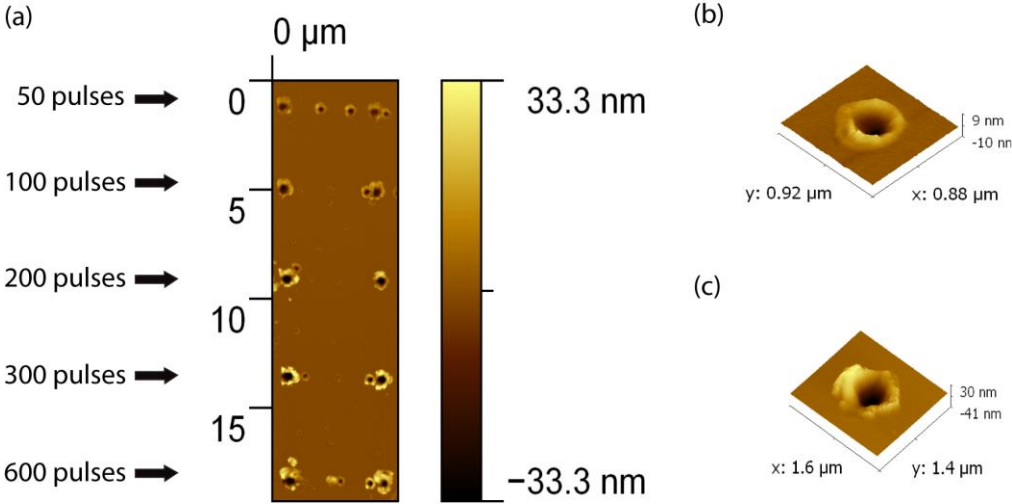
Figure 8: Nano-patterns generated on germanium using femtosecond laser (a) after 50, 100, 200, 300 and 600 laser pulses (b) after single pulse (c) after 200 laser pulses

Table 1: Nano-pattern sizes (average diameter of nano-pattern) generated on silicon and germanium

Number of laser pulses	Nanosecond Laser		Femtosecond Laser	
	Silicon (nm)	Germanium (nm)	Silicon (nm)	Germanium (nm)
50	Not observable		8±3	-15±5
100	Not observable		10±5	-30±10
300	6 ±2		20±10	-50±10
600	10 ±2		50±10	-55±20
900	15 ±3	-15 ±2		
1200	18 ±3	-20 ±2		
1800		-25 ±2		

Table 2: Nano-pattern sizes (average depth of nano-crater or height of nano-protrusion) generated on silicon and germanium

Number of Laser pulses	Nanosecond Laser		Femtosecond Laser	
	Silicon (nm)	Germanium (nm)	Silicon (nm)	Germanium (nm)
50	Not observable		500±50	500±50
100	Not observable		600±50	600±50
300	1200 ±200		800±100	700±100
600	1300 ±200		1000±50	900±100
900	1400 ±200	700±200		
1200	1400 ±200	800±200		
1800		900±200		

2) Near field laser-material interaction with metallic thin film coatings (Cr and Ag)

Chromium and silver were selected in the near field laser-material interaction with metallic materials considering their similar physical properties but significantly different surface reflectivity at $\lambda\sim$400-410 nm. The surface reflectivity of silver is ~10 times higher than that of Cr (Appendix A). Through comparing the nano-patterns generated on these two metallic materials the contribution of surface reflectivity in the near field laser-material interactions is expected to be revealed. The results from Cr and Ag with nanosecond and femtosecond laser pulses are listed as follows:

a) For nanosecond laser pulses

Cr: Nano-patterns were observed on the Cr film with ns laser after 100 laser pulses when E~1.8-2nJ. The shape of nano-patterns evolved from nano-craters to nano-protrusions gradually. This transition happened when the number of laser pulses

>200 (Figure 9). The diameter of nano-craters varied from 400nm to 600nm for 100-200 laser pulses (Table 3). Once the nano-protrusions were generated under larger number of laser pulses, the diameter of protrusions kept increasing with respect to number of laser pulses while the height increased slightly from 10nm to 20nm after 600 -1000 laser pulses (see Table 4).

Ag: No observable patterns were generated on silver surfaces even after 2000 laser pulses when E ~1.8–2.0 nJ or even under the damage threshold energy of NSOM probes (i.e. E ~2.5-3.0 nJ).
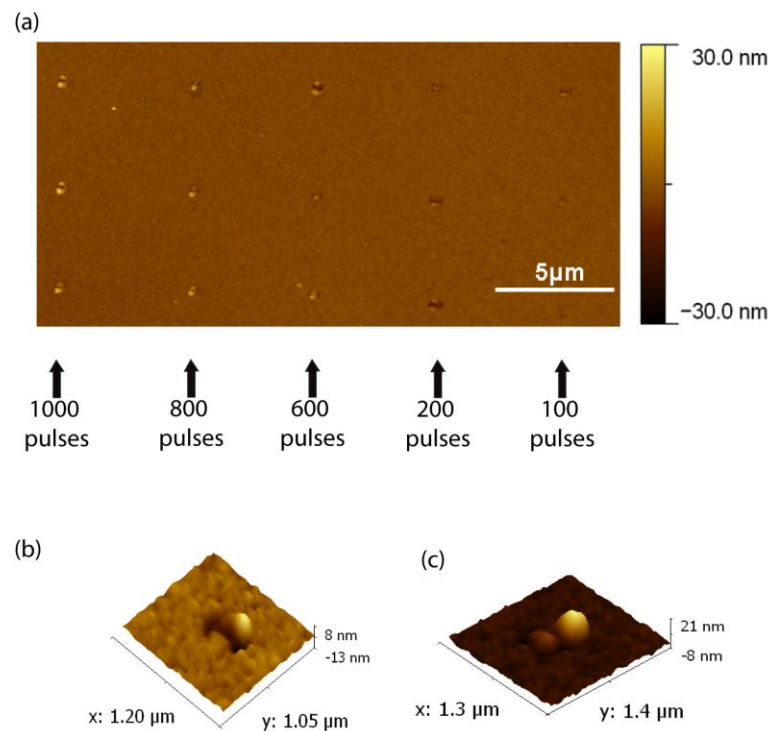
Figure 9: Nano-patterns generated on chromium using nanosecond laser (a) after 100, 200, 600, 800 and 1000 laser pulses (b) after 50 laser pulses (c) after 1000 laser pulses

b) For femtosecond laser pulses

Cr: Nano-pattern were observed on Cr targets with femtosecond laser pulses under all the laser energy studied (i.e., 1, 2 and 3 nJ). The patterns changed from nano-craters under single laser pulse to nano-protrusions for multiple laser pulses studied in air (i.e., 50, 100, 200, and 300 pulses) (see Figure 10). The nano-craters with single laser pulse have a diameter ~600 nm when E~2 nJ. The diameter and the nano-patterns showed little dependence on the number of laser pulses studied even when protrusions were formed (Table 3). However, the height of nano-protrusions increased from 40 nm to 55 nm when the number of laser pulses increased from 50 to 300 laser pulses (Table 4).
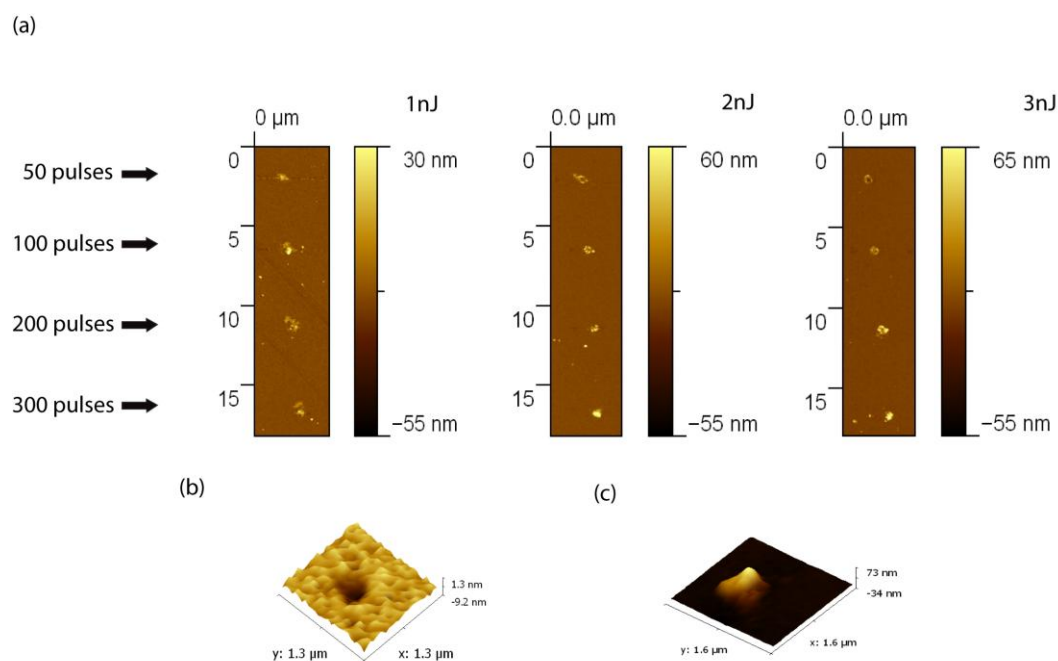
Figure 10: Nano-patterns generated on chromium using femtosecond laser (a) when input laser energy E~1nJ, E~2nJ, E~3nJ (b) after single pulse (c) after 300 laser pulses

Ag: No observable patterns were generated on silver surfaces even after 2000 laser pulses with all three input laser energies studied (i.e., ~1, 2, and 3 nJ). Note that 3 nJ is the maximum fs laser energy available to be coupled to the NSOM probe under the present experimental setup.

Table 3: Nano-pattern sizes (average diameter) generated on chromium and silver

Number of laser pulses	Nanosecond Laser		Femtosecond Laser	
	Chromium (nm)	Silver (nm)	Chromium (nm)	Silver (nm)
50		Not observable	600±100	Not observable
100	400±100	Not observable	700±100	Not observable
200	500±100	Not observable	800±100	Not observable
300	500±100	Not observable	900±100	Not observable
600	600±100	Not observable		Not observable
800	600±100	Not observable		Not observable
1000	600±100	Not observable		Not observable

Table 4: Nano-pattern sizes (nano-crater depths and nano-protrusion heights) generated on chromium and silver

Number of laser pulses	Nanosecond Laser		Femtosecond Laser	
	Chromium (nm)	Silver (nm)	Chromium (nm)	Silver (nm)
50	Not observable	Not observable	40±5	Not observable
100	-4±2	Not observable	50±5	Not observable
200	-6±2	Not observable	50±8	Not observable
300		Not observable	55±8	Not observable
600	10±2	Not observable		Not observable
800	15±4	Not observable		Not observable
1000	20±4	Not observable		Not observable

To obtain a general picture for the mechanisms responsible for nano-patterning which is the focus of this study, the influence of optical parameters on nano-pattern generation is

examined from the experimental data. From these connections, the generation of nano-patterns can be linked to the potential physical mechanisms which can qualitatively explain the obtained results under the conditions studied. In the following paragraphs, the influences of (a) laser pulse duration, (b) laser pulse energy, and (c) number of laser pulses (i.e, optical parameters) on the pattern generation with combination of NSOM systems and pulsed laser sources is discussed. The proposed physical mechanisms, which are responsible for nano-pattern generation in this study, are presented after the following discussion.

A. Contribution of laser pulse duration

For all the materials studied in this research, femtosecond laser generated patterns on targets with lower threshold energy compared with the nanosecond laser under the same number of laser pulses. In addition, patterns generated with fs laser were sharper with cleaner edges. In contrary to the lower damage threshold to the targets, the damage threshold of NSOM probes was significantly increased with fs laser (> 3 nJ) compared that with ns laser (<2.5-3 nJ).

Besides the contribution to the damage threshold of the NSOM probes and the targets the laser pulse duration also affected the chemical composition of the resulting nano-patterns on different targets. Si was selected as an example in this study. Though protrusions were generated on Si targets for large number of fs and ns laser pulses in air, the protrusion generated from fs laser could be entirely removed with BHF while the protrusions generated from ns laser could not be entirely removed with BHF. The BHF etching results suggest that the protrusions generated on Si wafer in air with ns laser had components in addition to SiO_2. Through the additional examination of the protrusions generated with ns laser (i.e. through EDS, XRD and TEM scanning), it was found that these protrusions were composed with a significant amount of nano-crystalline Si which did not appear in fs results. A detailed explanation for the formation of these unique protrusions which have not been observed before is provided at the end of this section.

B. Contribution of number of laser pulses

For all the materials studied in this research (i.e., Ge, Si, and Cr), the size of the nano-patterns, more or less, increased with respect to the number of laser pulses. However, the pattern shapes may change with respect to number of laser pulses (note that this statement is not true for silver on which no patterns were observed). The change in the shape of the nano-patterns happened in Si with fs laser pulses and Cr with both ns and fs laser pulses. For the above three experimental conditions, the shape of patterns evolved from nano-craters to nano-protrusion when the number of laser pulses increased. The major difference between Si/Cr group (on which the resulting nano-pattern shape showed dependence on the number of laser pulses) and Ge target (on which the resulting nano-pattern shape showed no dependence on the number of laser pulses) was oxidation compounds of each of the groups. Stable oxidation compounds (i.e., $SiO2$ for Si and $Cr2O3$ for Cr) were formed on Si and Cr surfaces under low temperature heating (i.e., $<\sim500$ K). However, close to melting temperatures were required for forming $GeO2$ on Ge surfaces.

C. Contribution of laser energy

For ns experiments, fixed pulsed laser energy (i.e., E $\sim1.8 - 2.0$ nJ) was utilized because no patterns were observed when E$<1.6 - 1.8$ nJ along with the fact that the NSOM probes were damaged when E$> 2.5 - 3.0$ nJ. Experiments with femtosecond laser were conducted under three different energies namely E~1, 2 and 3 nJ. Note that the NSOM probes remained healthy under all three energy levels studied with fs laser. An increase in the pattern height/depth was observed when the input fs laser energy was increased. The pattern shapes and diameters, on the other hand, showed little dependence on the fs laser energy for the experimental conditions studied.

Based on the observed contribution of optical parameters listed above, a physical picture which is an extension from traditional microscale laser-material interaction is established

to explain the optical/thermal energy transport from the NSOM probe to the targets along with the resulting nano-pattern generation. These physical pictures fits with the experimental data obtained in this study and allows us to predict the results for future experiments under similar experimental conditions. A description of this physical picture is as follows:

When ns laser was applied, significant light dissipation (mainly around the NSOM tip) is converted into the thermal energy of the NSOM probe considering >99.9% of optical energy is dissipated into heat during the transport within the NSOM probe [6], the NSOM probe maintains a very high temperature around the tip while carrying intense ns laser pulses [25,26]. As a result, in addition to the optical energy transport from the NSOM probe to the target through near field effects, there is a considerable amount of thermal energy transport from the NSOM probe to the target during the experiments when ns laser pulses are applied. This additional thermal energy transport induced by ns laser pulses can melt the sample (which was observed on Si targets) or even the metal cladding of the NSOM probes (see Figure 11) as was observed in this study when light intensity is above the threshold.
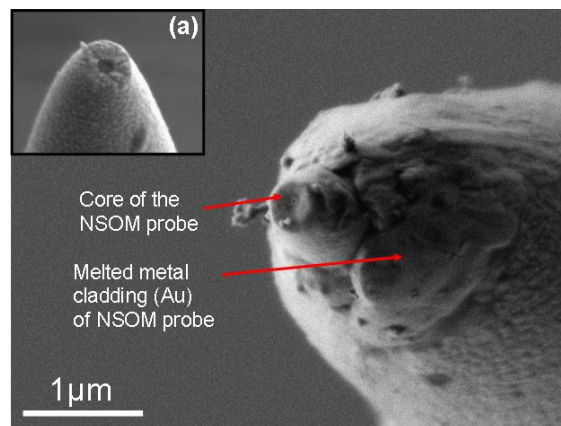
Figure 11: SEM image of NSOM probe with nanosecond laser induced thermal damage indicating gold melt region obtained from EDS analysis (inset) new NSOM probe

When fs laser was applied, the light fluence at the target with fs laser is ~10^4 times higher than that with ns laser under the same E values. Due to the extremely high laser

fluence associated with fs laser pulses, non-linear (e. g., multiphonon) light absorption especially for semiconducting materials is important. Strong surface heating or even coulomb explosion [27] on semi-conducting materials can be induced through non-linear optical absorption compared with ns laser cases. As a result, patterns are formed on targets will lower threshold energy compared with that under ns laser pulses. In addition to the non-linear optical absorption, the ultrashort pulse duration with fs laser reduces the characteristic time for thermal diffusion (or heat affected zone, HAZ) in the targets. The smaller thermal diffusion region provides a better confinement of thermal energy, which causes higher temperature in a small region around the laser spot when fs laser is applied. Consequently, the pattern generation threshold is further reduced with femtosecond laser if we consider the thermal effects induced by fs laser pulses. The physical picture for fs laser-material interactions explains the reduction of the damage threshold of Cr, Si and Ge targets in this study (which are the three targets on which nano-patterns were observed) when fs was applied compared with ns laser results.

Besides lowering the damage threshold of the target, due to the ultrahigh photon fluence associated with fs laser pulses, photoelectron emission can be induced at the metal cladding of NSOM probes due to the high photon fluence when fs laser pulses are carried through the NSOM probes [28]. The emission of electron carries a significant amount of absorbed EM energy in the metal cladding to the surrounding. As a result, the NSOM probes can maintain a low temperature when they are operating with fs laser pulses. Consequently, much high energy fs laser pulses can be transported with NSOM probes without any thermal damages compared with ns laser cases. This statement is supported with the SEM observation of the NSOM probes after operating with fs and ns laser pulses.

Three main mechanisms [29] can be induced on the targets after absorbing energy from NSOM probes and are responsible for the nano-pattern generation in this study. These three mechanisms are (a) nano-scale laser ablation of the target, (b) nano-scale oxidation

resulting from nano-scale heating of the target, and (c) nano-scale recrystallization resulting from nanoscale melting of the target. Nano-craters on the target can be formed through nano-scale laser ablation while nano-protrusion can be formed either through nano-scale oxidation or nano-scale recyrstallization of the targets. Note that more than one mechanism may attribute to the nano-pattern formation in each experimental condition. The pattern formation induced by multiple mechanisms is especially important when more than one laser pulses is applied.

When more than one laser pulses were applied to the targets, change in size and shape of the nano-patterns as function of number of laser pulses can be understood from following three scenarios,

a) Nano-crater is first generated for single or few laser pulses due to nanoscale laser ablation. The crater depths keeps increasing with respect to the number of laser pulsed since the additional laser ablations keep removing material from the target. Nano pattern formation following this scenario was observed on targets on which oxidation layers are difficult to be formed at low temperatures (e.g., Ge with ns and fs lasers). This is explained in Figure 12.
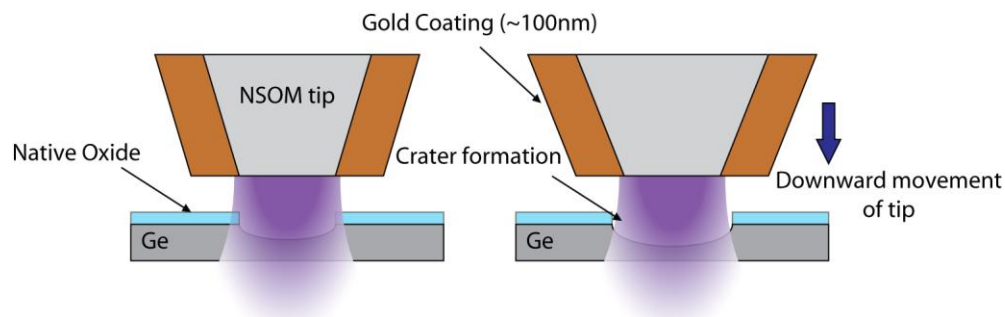
Figure 12: Schematic showing nano-crater generation on germanium after 50 laser pulses and increase in the crater size with increase in number of laser pulses

b) Nano-crater is first generated with single pulses due to nanoscale laser ablation. Surrounding the ablated crater is an oxidation layer on the heated target. The thickness of the oxidation layer increases with respect to the number of laser pulses.

As a result, the separation between the NSOM probe and the intrinsic target becomes larger and larger when the number of laser pulses is increased. The semiconducting oxides (or metallic oxides) act as a buffer layers between NSOM tip and the intrinsic target. Consequently, near field light intensity at the intrinsic target surface from the following laser pulses becomes weaker because of the thicker oxidation layer, which increases the separation between the NSOM tip and the intrinsic target (see Figure 13). After certain number of laser pulses, the effective light intensity at the intrinsic target is not enough to induce a nano-scale laser ablation. After that only oxidation resulting from laser heating of the target can occur and dominates the patterns formation, which causes the transition of pattern shape from nano-craters to nano-protrusions. Nano-pattern formations following this trend were observed on targets on which oxidation layers are formed under low temperatures (e.g., Si with fs; Cr with ns and fs).
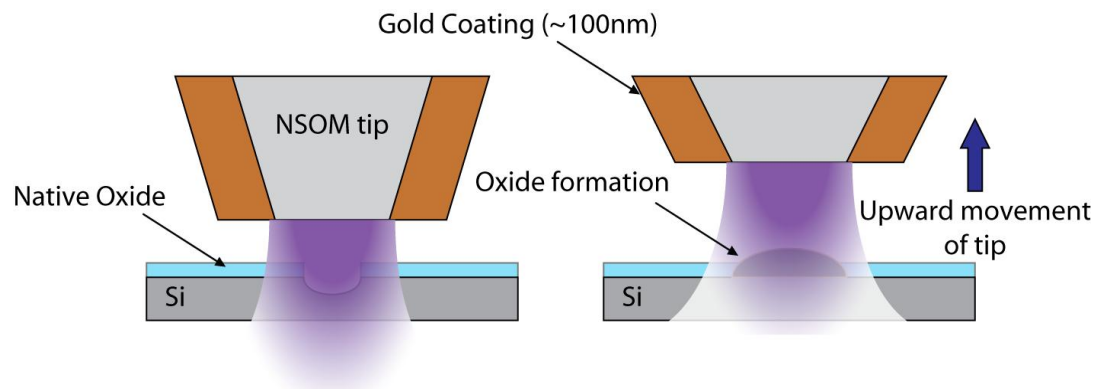
Figure 13: Schematic showing nano-crater generation on silicon after 50 laser pulses and change in pattern shape from nano-crater to nano-protrusion with increase in number of laser pulses when femtosecond laser is used

c) Nano-protrusion is first generated for single or few laser pulse since the energy is not enough to ablate the target. The protrusions can be formed either from nanoscale oxidation [12] or nanoscale melting and recrystallization of the target. The height of protrusion increases slowly with respect to the number of laser pulses due to the

increased separation distance between the NSOM probe and the intrinsic target when the protrusions were formed. Nano-pattern formation following this trend was observed on targets with high ablation threshold and low oxidation temperature (e. g., Si with ns).

When the laser energy is increased, as long as it is higher than the pattern generation threshold, the efficiency of ablation and/or oxidation is enhanced. Deeper craters or higher protrusions were generated on the same target through ablation and oxidation separately when the fs laser energy is increased. Note again that the ns laser energy was not varied in this study since the damage threshold of the target was very close to the damage threshold energy for NSOM probe.

The above physical picture describes the energy transport from NSOM probe to the target along with the target response and associated nano-pattern generation as functions of optical conditions and the chemical properties of the target material. The physical picture does fit with the experimental data obtained in this research under all the conditions studied.

From comparing the results on different targets under the same optical conditions, the contribution of optical properties of different materials on nano-pattern formation can be revealed. The first example is the significant differences in pattern size and shapes on Si and Ge. Both materials have similar optical reflectivity under the wavelength tested. In addition, both materials have similar thermal properties (i.e., thermal conductivity and heat of vaporization (Appendix A). However, because of the smaller band gap of Ge (~6 eV) compared with Si (~11 eV), Ge has absorption coefficient ~7 times higher than that of Si (Table 1). A surface type light absorption occurs in Ge compared with a more volumetric type light absorption in Si. The stronger light absorption in a smaller volume induces a strong mass removal during near field laser material interaction on Ge compared with that on Si under the same laser conditions (see Figure 14). As a result, larger craters were observed on germanium surfaces under all the experimental

conditions studied (note that there are even no craters observed on Si surfaces under certain experimental conditions).
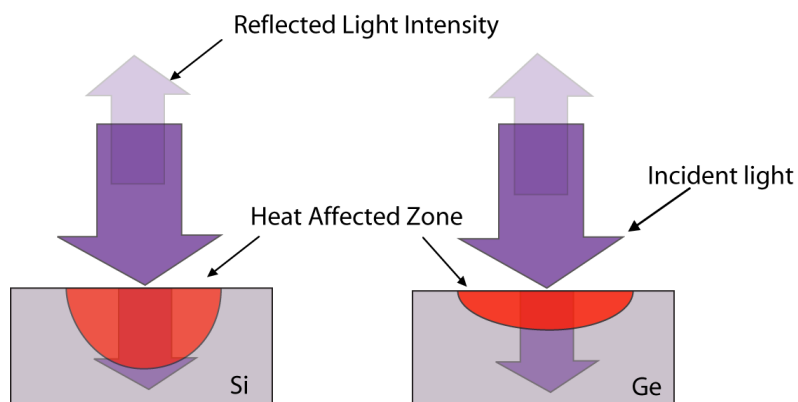
Figure 14: Schematic showing effect of sample absorption coefficient on nano-pattern generation

Another example obtained in this study was the dramatic difference in the pattern formation on Cr and silver. No pattern was observed on Ag surfaces under all the experimental conditions studied. The zero pattern generation on silver in this study can be attributed to its extremely high surface reflectivity (~90%) compared with Cr (<~5%) at λ~400-410 nm (Appendix A). Little amount of incident light from the NSOM tip enters the silver target due to this extremely high surface reflectivity, which prevents nano-pattern generation (see Figure 15).
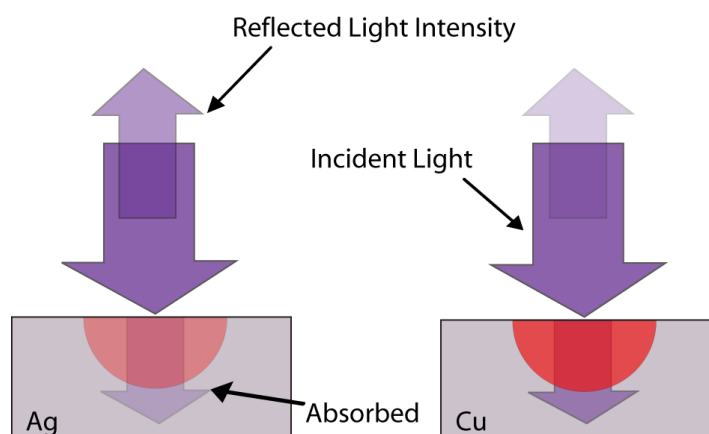
Figure 15: Schematic showing effect of sample surface reflectivity on nano-pattern generation

A supplementary ns laser experiment was conducted on Cu in air in order to verify the physical picture that was obtained in this study for understanding the nano-patterning on targets as a function of optical/chemical properties of the targets. Cu has similar thermal properties compared with silver and Cr. Like Cr, Cu has very low surface reflectivity ($\tau \sim 0.08$) at $\lambda \sim 400\text{-}410$ nm. However, compared with Cr, copper oxide can only be formed efficiently under high temperature [30]. Therefore, because of the absence of thick oxidation layers, nano-craters were expected on Cu under all the experimental conditions studied. The supplementary experimental results did fit with the prediction. When ns laser was applied to the Cu target with NSOM, nano-craters with diameter ranged from 300 to 600 and depth ranged from 5 nm to 7 nm were observed after 900 to 1800 number of laser pulses when $E \sim 2$ nJ (Figure 16 & Table 5).

Table 5: Nano-crater depths and diameters on copper

Number of Laser Pulses	Nano-crater diameter (nm)	Nano-crater depth (nm)
900	300±100	-4±2
1200	500±100	-5±2
1800	600±100	-7±2
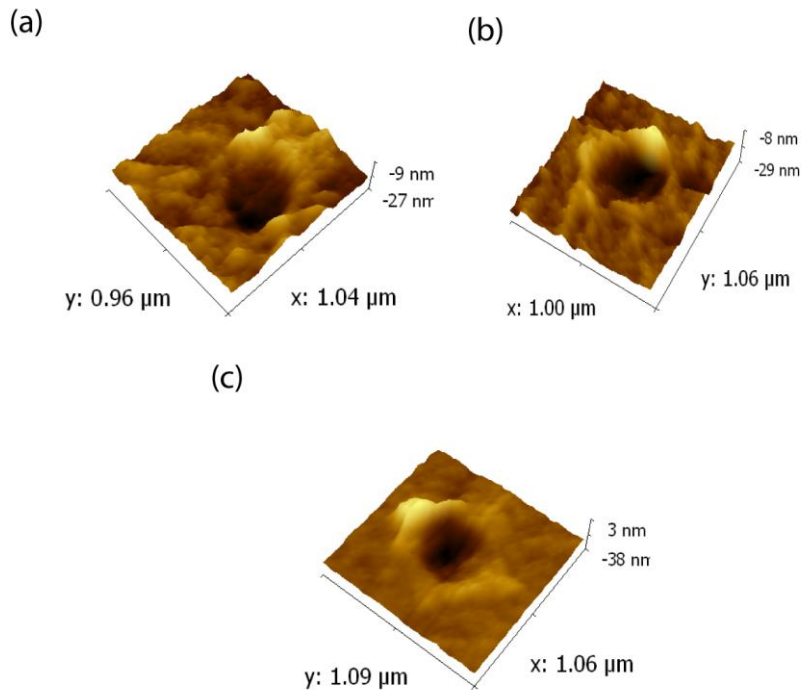
Figure 16: Nano-patterns generated on copper using nanosecond laser after (a) 900 laser pulses (b) 1200 laser pulses (c) 1800 laser pulses

Analysis of composition of nano-patterns generated on intrinsic silicon wafer using nanosecond laser:

Characteristics of the nano-patterns generated on silicon wafer in air and in argon environments separately through a combination of a NSOM probe and ns laser pulses are listed as follows.

1. When air was used as the background gas, nano-protrusions were generated on silicon wafer surfaces after multiple nanosecond laser pulses for input laser energy of ~1.8-2nJ. The diameters of protrusions increased from 1000nm to 1200 nm and heights increased from 6 to 15 nm when the number of laser pulses increased from 600 to 900 (Figure 17). Note that the protrusions formed on the silicon surface in air cannot be dissolved with BHF solution, which is different from those obtained with fs laser as in the previous study [12]. Therefore, these nano-protrusions generated

in air were not composed with SiO2 only.

2. When argon was used as the background gas, similar nano-protrusions were generated on the silicon surface after multiple nanosecond laser pulses for input laser energy of 1.8-2nJ. These protrusion results with ns laser in argon is entirely different from the craters results obtained with fs laser in argon in previous study [12]. The diameter of the protrusions increased from 1000 to 1100 and the heights changed slightly from 2 to 4nm when the number of laser pulses increased from 600-900 (Figure 17). However, unlike the protrusions formed in air, these much smaller protrusions could be completely etched into nano-craters after immersing them into BHF solution. The diameter of these craters obtained after etch was ~250 nm with depths ~4-6nm.

Since no nano-craters were observed on the targets even in Ar after thousands of laser pulses, it is concluded that laser ablation is not one of the major pattern generation mechanisms when ns laser pulses were applied on Si targets. Note that the selected ns laser energy (E~1.8 - 2 nJ) is very close to the maximum laser energy which can be afforded with the selected sub-diffraction limit NSOM probe.
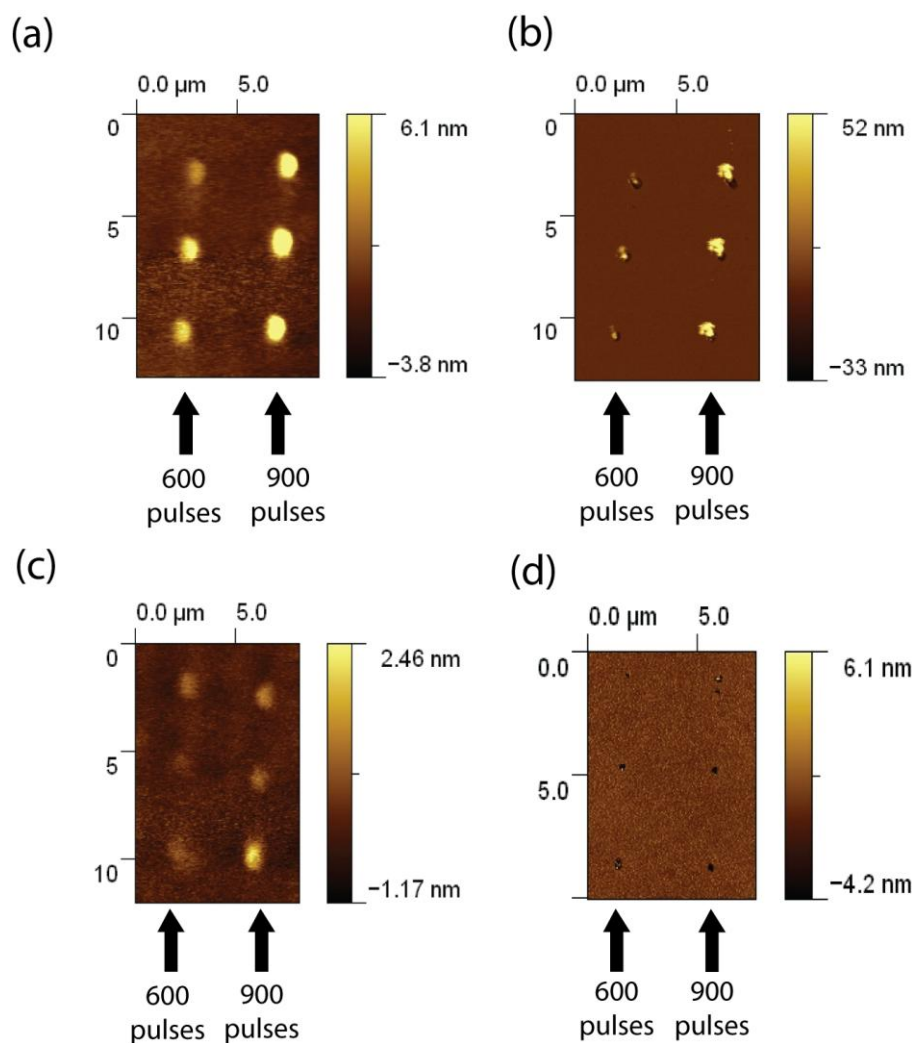
Figure 17: Nano-patterns generated on silicon using nanosecond laser (a) in air before etching using BHF(b) in air after etching with BHF (c) in argon before etching with BHF (d) in argon after etching with BHF

To determine the formation mechanism of nano-protrusion with ns laser pulses, the chemical compositions of the protrusions was first examined. Three chemical elements exist around the sub-diffraction limit confined laser spot during the experiments, namely, gold (the metal cladding of the NSOM probe), SiO_2 (the core of the NSOM probe and the intrinsic oxidation layer of the silicon wafer), Si (the target material). EDS and XPS were applied to check the chemical composition of the nano-protrusions. Both EDS and spectrums showed no evidence of gold element on the target (see Figure 18). Therefore,

the protrusions formed on the silicon surface in air which cannot be fully dissolved with BHF should be due to a presence of a significant amount of pure silicon. The protrusion formed on the silicon surface in Ar which can be fully dissolved with BHF should be composed mainly with SiO_2.
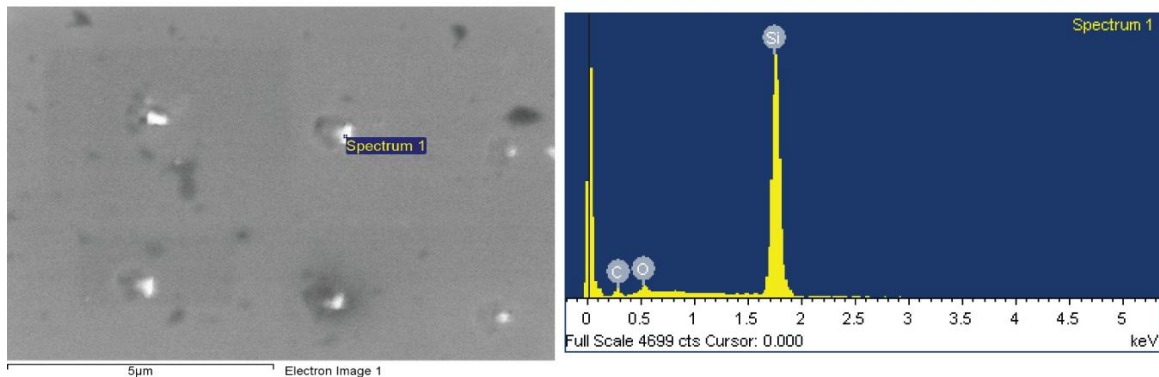
Figure 18: EDS spectrum showing chemical composition of the protrusions. The spectrum analyzes the composition of the marked area on the SEM image

To further understand the generation mechanisms of nano-protrusions under nanosecond laser pulses, large protrusions (~120 nm in height and ~1 μm in width) were generated in air after ~3000 laser pulsed when E~2.8 nJ. The nano-protrusions were diced with Focused Ion Beam (FIB) and then examined with TEM (Figure 19). From the TEM images, the nano-protrusion is actually a hump of a large recrystallized region composed with SiO2 and nano-crystalline silicon (nc-Si). This recrystallized region is separated with the Si base through a flat and uniform SiO_2 layer. Though the SiO_2 layer is pretty flat at most regions, the TEM image showed a very slight extension of the SiO_2 layer into the Si base at the region beneath the centers of the nano-protrusions. The diameter of this additional extend SiO_2 region into the Si base is ~100-200 nm with depths <~10 nm into the Si base.
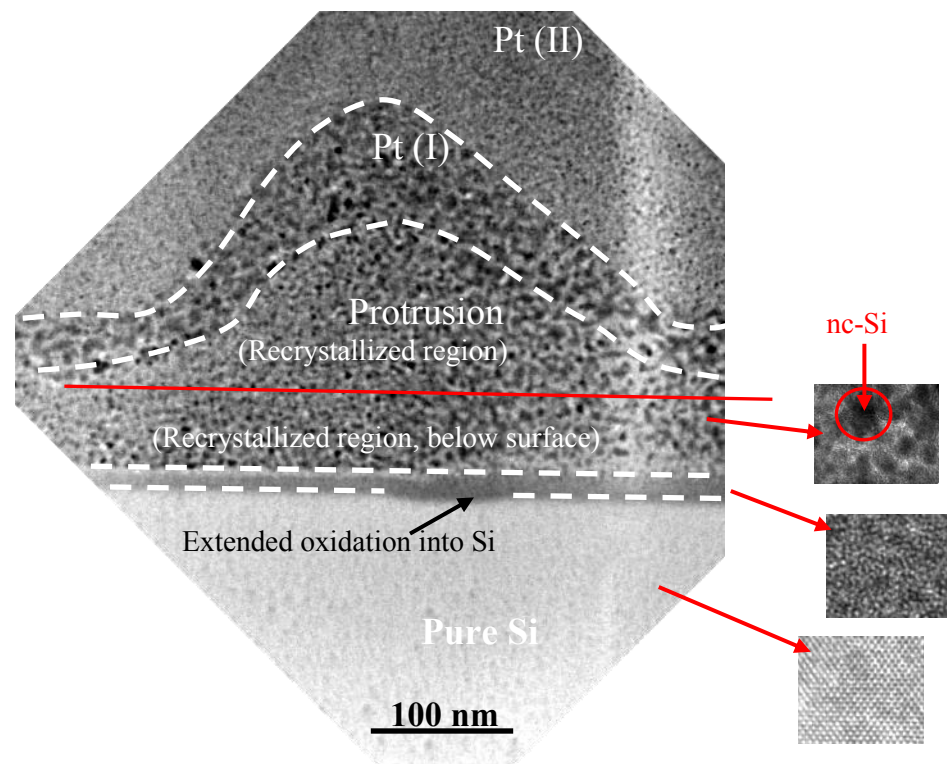
Figure 19: TEM image of cross-sectional view of the nano-protrusion after dicing using FIB. The image shows four different regions. The dark spots correspond to the nano-crystallized silicon. The top platinum layer has been deposited to protect the sample during FIB dicing process

The formation of the nc-Si cannot be due to a pure oxidation process. However, through fast melting and recrystallization of existing SiO_2 region, abundant nc-Si can be formed in recrystallized SiO_2. One similar example is the microscale direct laser heating (annealing) of silicon rich (or pure) SiO2 with ns (or longer duration) laser pulses, which results in micro-scale protrusions (>10 – 20 μm) composed with nc-Si and SiO_2 [31-33]. It is suggested that a similar mechanism can be attributed to the formation of nano-protrusions composed with SiO_2 and nc-Si in this study. The formation of large protrusion on Si in air with ns laser pulses can be understood from a sequence of physical processes as follows:

I. The intrinsic SiO_2 layer is melted and recrystallized into a small protrusion (composed with SiO_2 and nc-Si) resulting from the optical/thermal energy

transport from the NSOM probe to the target during and after the first ns laser pulse.

II. An additional thin SiO2 layer is formed beneath the recrystallized region due to the oxygen diffusion into the Si base shortly after the ns laser pulse.

III. The recrystallized region along with the underlying SiO2 layer from previous laser pulses are melted and recrystallized again by the following successive laser pulses. As a result, the size of the nano-protursion is increased after each laser pulse in air. More and more nc-Si appears in the nano-protrusion after each laser pulse, which prevents the nano-protrusions from being entirely etched with BHF.

For experiment in Ar, since there is no continuous oxidation of the Si base as described in step II due to the lack of oxygen atoms, the growth of the protrusions height is very limited compared with the results in air. Also, the size of the protrusion in Ar does not increase with respect to the number of laser pulses. Due to the presence of much less nc - Si in the protrusions formed in Ar, the protrusions could be entirely removed with BHF. When the protrusion was removed with BHF, nano-craters of diameter ~100-200nm and depth ~4-6 nm were revealed at the end of the etching process. These shallow craters correspond to the shallow extension of SiO2 layer into the Si base as indicated in the TEM image. The formation of this additional shallow SiO2 can be attributed to the laser enhanced oxygen diffusion from the recrystallized region to the Si, since it overlaps with the regions where strong light intensity appears during the experiment.

The lack of melting and recrystallization mechanisms in nano-pattern formation in previous fs experiments can be understood from the significant heating of NSOM probes with intense ns laser pulses compared with fs laser pulses. Though a lower ns laser energy (E~1.8-2 nJ) was applied in this study to prevent the damage of the NSOM probes, the temperature of the probe can still approach the melting (~1337 K) or even boiling temperature (~3129 K) during the experiment [25]. The hot NSOM probe can transport its thermal energy directly to the target surface through conduction and

radiation. The strong thermal energy transport from the NSOM probe to the target can result in melting and recrystallization of the target forming nano-protrusions. Such strong thermal energy transport does not exist in experiments with fs laser pulses, which prevents the formation of the melting and recrystallization structure in the previous study.

3.3 Summary

Near field nano-patterning through NSOM probes was conducted on selected semi-conducting targets (i.e. Si and Ge) and metallic targets (i.e. Cr, Cu and silver) at λ ~400-410 nm. The contributions of laser pulse duration (i. e., fs vs. ns), number of laser pulses, and laser energy on different targets were studied with controlled experiments in this research. Based on the results, fs laser did not cause any damage to the NSOM probe under high laser energy while thermal damages of NSOM probe was observed with ns laser pulses when E>2.0-2.5 nJ. Furthermore, because of the non-linear optical absorption along with a smaller HAZ, the damage threshold of targets with fs laser pulses (<1nJ) is much lower than that with ns laser pulses (~1.8-2.0 nJ) when they are delivered with NSOM probes to the targets.

The formation of the nano-patterns on different targets can be explained with nanoscale laser ablation, nanoscale oxidation and nanoscale melting/recrystallization of the targets. The increment of input laser energy merely enhanced the pattern formation mechanisms and the resulting size of the patterns on the targets under all the experimental condition studied. The number of laser pulses, however, can change the size and the shape of the resulting patterns on different targets. For materials on which both nanoscale ablation and nanoscale oxidation dominate nano-pattern generation (e.g., Si & Cr), the contribution of nano-scale ablation become weaker in the following laser pulses due to a thick oxidation layer from previous laser pulses. The thick oxidation layer reduces the light intensity at the intrinsic target and prevents further nanoscale laser ablation on the targets after certain number of laser pulses.

Besides the contributions of the optical (laser) conditions on nano-pattern formation, the optical properties of the targets can significantly change the resulting nano-patterns obtained from a combination of NSOM probes and pulsed lasers. Targets with higher absorption coefficient formed larger craters due to a stronger energy absorption within a confined area on the targets. Targets with higher surface reflectivity, on the other hand, experience limited laser-material interaction during each laser pulse, which results in small or even no craters after the experiments. Note that when nanosecond laser was combined with a sub-diffraction limit NSOM system for nanoscale laser patterning on silicon wafer, laser ablation was no longer one of the dominant pattern generation mechanisms on Si targets. Instead, the nano-protrusions were formed primarily due to the melting and recrystallization of Si target along with the possible oxidation of Si base when O_2 was present in the background gas. These unique nano-protrusions were composed with SiO_2 and a significant amount of nc-Si which was not observed in previous fs experiments. The melting and the recrystallization of the target can be attributed to the strong heating of the NSOM probes when they are operating with ns laser pulses. The hot NSOM probes transport significant amount of thermal energy transport to the target.

4. NANO-LITHOGRAPHY WITH MICRO ZONE PLATE – THEORY AND FABRICATION

4.1 Zone Plate Design

The zone plate in this study has been designed based on the theory of focusing using a traditional Fresnel zone plate. Consider a plane monochromatic light wave incident on the zone plate from the left. The location and width of the zones is determined based on the equal optical length principle. In this design, the central aperture is considered to be opaque, though a transparent central zone is also possible. Based on the Huygens principle [34,35], each point on the slit will act as a point source for secondary wavelets. If the path difference between the light from two adjacent transparent zones is exactly λ, the light from the different transparent zones will interfere constructively at the focus point.

Consider a regular zone plate following the above design criteria is shown in Figure 20. The optical path of light from the center of the zone plate is denoted by f (which is equal to the focus length). Since the center zone is blocked, the width of the second zone must be designed such that the light from the second zone destructively interferes with the light from the central zone. In other words, light from the point r_1, in the figure (Figure 20), should have a path length of $(f+\lambda/4)$ and light from r_2 should have a path length of $(f+3\lambda/4)$. Hence the width of the first zone is given by

$$\Delta r = r_2 - r_1 = \sqrt{\left(f + 3\lambda/4\right)^2 - f^2} - \sqrt{\left(f + \lambda/4\right)^2 - f^2} \qquad (3.1)$$

The width of the remaining zones can be calculated in a similar manner. Note that the above equation considers only the first order focus of the designed zone plate, and neglect the higher order light focusing at longer focus distances. This approximation is good when the NA is >0.5, which falls in the range of the zone plate design used in this study [34].
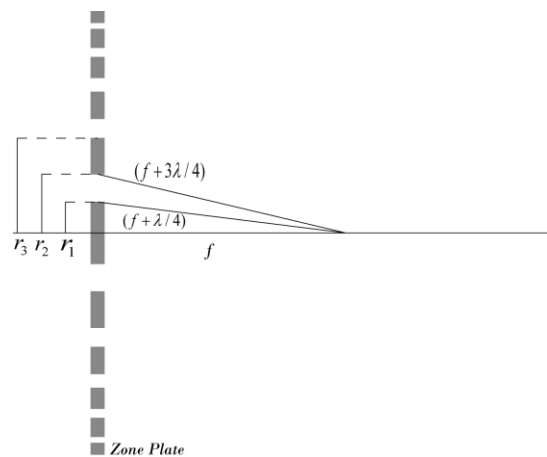
Figure 20: Schematic showing construction of zones of Fresnel zone plate

If we consider the incident light wavelength to be 409 nm and the focus distance to be ~ 3 μm, the following table shows the radial location of the zone centers (r_n) and the width of the opaque and transparent zones based on (4.1).

Table 6: Zone width and radius

Zone	Focal Length (μm)	Wavelength (μm)	Dr(μm)	r_n(μm)
1	3	0.409	0.600989	1.090403
2	3	0.409	0.433624	1.607709
3	3	0.409	0.36792	2.008481
4	3	0.409	0.33112	2.358001
5	3	0.409	0.307263	2.677192
6	3	0.409	0.290459	2.976053
7	3	0.409	0.277966	3.260265
8	3	0.409	0.268314	3.533405
9	3	0.409	0.260641	3.797883
10	3	0.409	0.254402	4.055404
11	3	0.409	0.249238	4.307224
12	3	0.409	0.244899	4.554292
13	3	0.409	0.241209	4.797346
14	3	0.409	0.238037	5.036969
15	3	0.409	0.235285	5.27363
16	3	0.409	0.232878	5.507711

Based on equation (4.1), for a traditional Fresnel zone plate, the zone width gradually approaches $\lambda/2$ with the increase in the number of zones (see Figure 21). The plot of the zone width as a function of zone number is shown below.
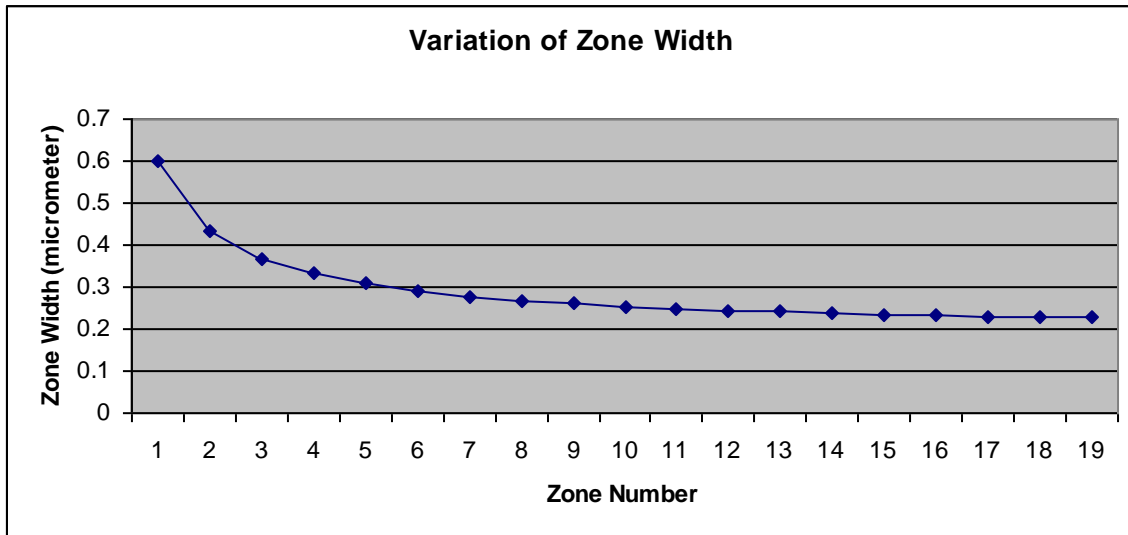
Figure 21: Plot of variation of zone width with number of zones

A schematic drawing of the design of the zone plate used in the fabrication of this study is provided in Figure 22.
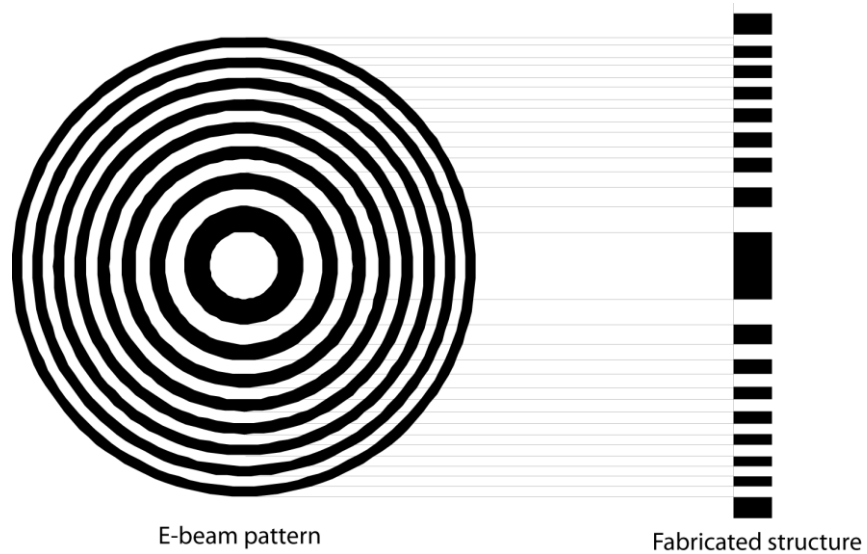
Figure 22: Comparison of zone-plate used during e-beam writing and image of final fabricated structure

4.2 Zone Plate Focusing Analysis

The numerical aperture (NA) of far field optical device is defined as

$$NA = \sin \theta \tag{3.2}$$

where θ is the half angle measure from the focus of the lens. A higher numerical aperture corresponds to a larger angle of convergence. The resolving power of an optical device is related to its numerical aperture can be approximated as

$$R = \frac{0.61\lambda}{NA} \tag{3.3}$$

For a Fresnel zone plate the NA can be expressed as

$$NA = \frac{R_N}{\sqrt{\left(R_n^2 + f^2\right)}} \tag{3.4}$$

where R_N is the radius of the last zone of the zone plate and f is the design focal length. For a zone plate with dimensions given Table 6, NA ~0.89. The corresponding smallest spot can be generated with the zone plate, theoretically, is ~280nm.

In order to verify the zone plate dimensions calculated based on equal optical paths, the Rayleigh-Sommerfeld diffraction integral was used to determine the focal length of the designed zone plate analytically (The Rayleigh-Sommerfeld theory provides a simpler integral equation if we consider an infinitely distant point source producing plane wave illumination at the zone plate plane compared to Kirchhoff Theory) [36]. According to the scalar diffraction theory, the electric field diffraction pattern at various points on a plane denoted by (x,y,z) due to an aperture located on a plane with points denoted by (x',y',z') can be expressed as a Rayleigh-Sommerfeld integral (see Figure 23). Note that the Rayleigh-Sommerfeld diffraction integral can be assumed to be valid as a first order approximation as long as the distance from the zone plate (z in the equation) is much larger than the wavelength, which is approximately true in this study [36].
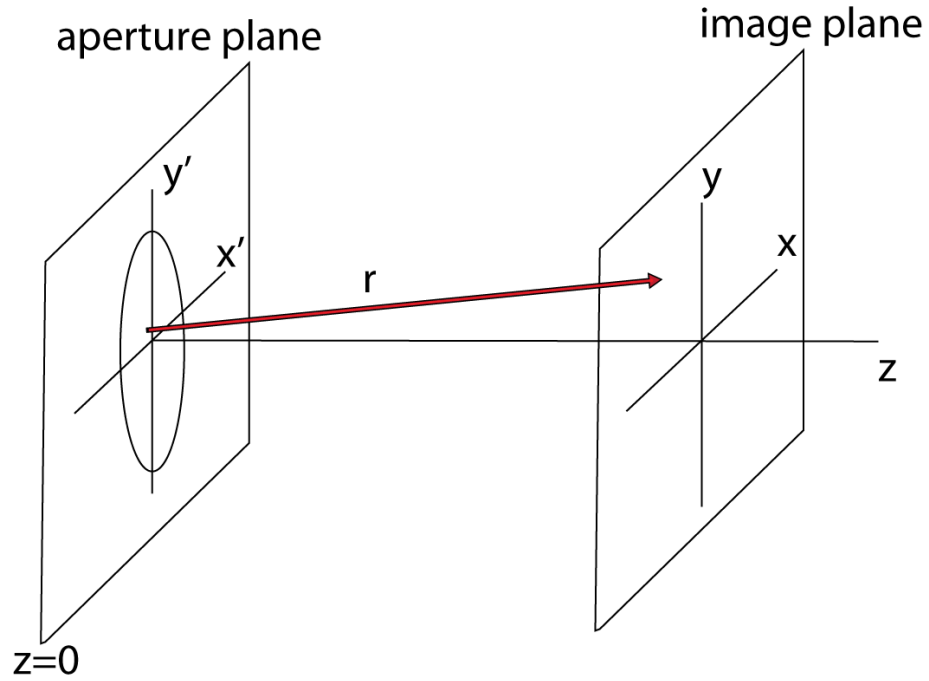
Figure 23: Diffraction geometry showing image plane, aperture plane and co-ordinate system used

$$E(x, y, z) = \frac{1}{i\lambda} \iint E(x', y', 0) \frac{e^{ikr}}{r} \cos\theta \, dx' dy' \qquad (3.5)$$

where i is the imaginary unit and $r = \sqrt{(x-x')^2 + (y-y')'^2 + z^2}$ as shown in the figure. The integral can be simplified to

$$E(x, y, z) = \frac{z}{i\lambda} \iint E(x', y', 0) \frac{e^{ikr}}{r^2} \, dx' dy' \qquad (3.6)$$

Physically, the integral describes the field at the image plane as a superposition of diverging spherical waves given by e^{ikr}/r, originating from point sources located at every point on the aperture, as stated by Huygens Principle. To verify the focal length of the zone plate for the design in Table 6, the field distribution along the z axis has to be determined. Hence this equation can be simplified in cylindrical coordinates as,

$$E(z) = \frac{z}{i\lambda} \int E(r) \frac{e^{ik\sqrt{r^2+z^2}}}{r^2 + z^2} \, dr \qquad (3.7)$$

where *r* denotes the radial direction on the aperture plane. Since the zone plate has eight zones, this integral has to be split into 8 different parts corresponding to each zone. The radius values of each of these parts were obtained from Table 6 and the integral was solved using Maple®. The intensity variation with distance from the zone plate is shown in the Figure 24.
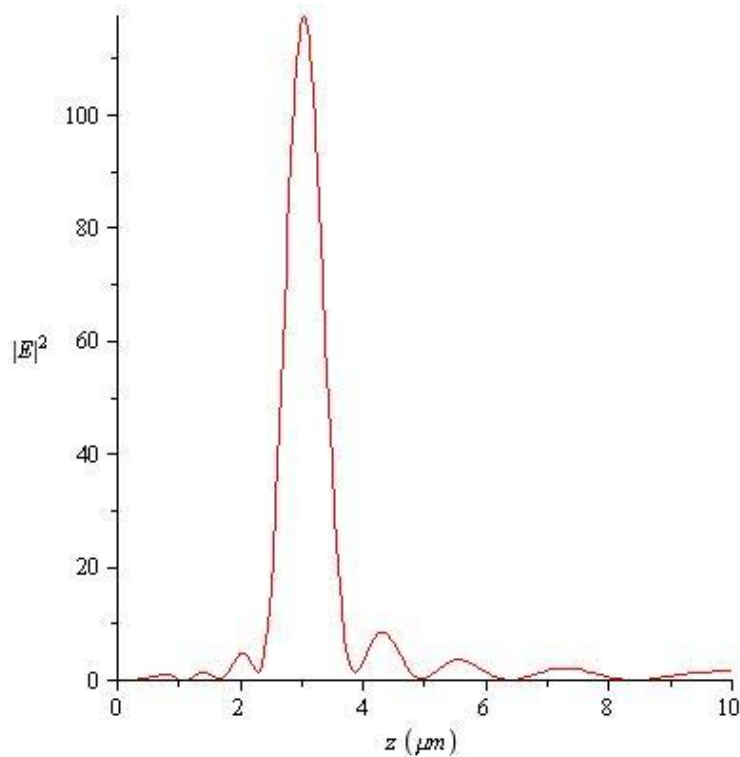
Figure 24: Plot of intensity distribution along the centerline of the zone plate showing focus spot at z=3μm

The analytical solution to the Fresnel integral also predicts a focus point at *3μm* from the zone plate. Since the peak intensity occurs at *3μm* from the zone plate (see Figure 25) , the Rayleigh-Sommerfeld integral can be numerically solved to determine the intensity distribution at a distance of *3μm* from the zone plate. Due to cylindrical symmetry of the zone plate, the intensity distribution in the image plane is also independent of *θ*. Therefore the integral simplifies to

$$E(r) = \frac{z}{i\lambda} \int\limits_{zones} \int\limits_{0}^{2\pi} E(r',\theta',0) \frac{e^{ik\sqrt{(r-r'\cos\theta)^2+(r'\sin\theta)^2+z^2}}}{(r-r'\cos\theta)^2+(r'\sin\theta)^2+z^2} d\theta' dr' \qquad (3.8)$$

where the primed terms denote the aperture plane and the unprimed terms denote the image plane. Since the intensity distribution in the image plane has cylindrical symmetry, the angle θ, has been taken to be 0 for convenience. The integral was numerically solved in Maple and the intensity variation from $r=0$ to $r=5\mu m$ is shown in Figure 25. The plot shows a peak intensity at $r=0$ and side-lobes at $r=1.5$ and $3\mu m$. However the intensity at the peak is almost 10 times higher than the side lobes. Also, the FWHM can be seen to be ~220nm from the figure. Comparing this value with the resolving power of the designed zone-plate from(3.3), it can be seen that the Rayleigh-Sommerfeld diffraction theory predicts a smaller focus spot.
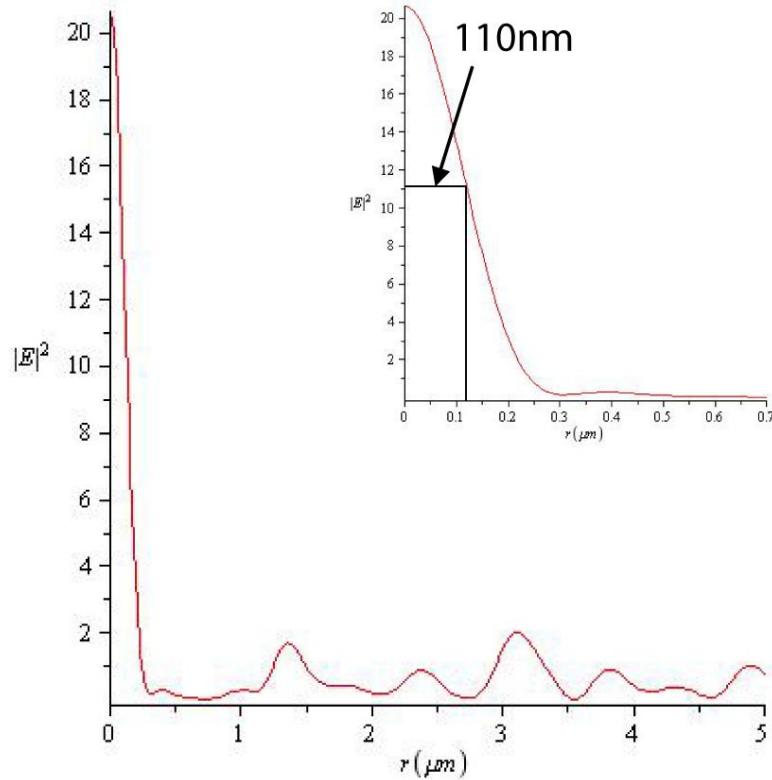
Figure 25: Plot of intensity distribution at z=3μm showing a peak at the focus spot corresponding to r=0 in the image plane and side lobes at r~1.5μm (inset) FWHM ~220nm

A. Improving the focusing efficiency of a Traditional Fresnel Zone Plate

A number of techniques have been proposed to improve both the focusing and the energy transport efficiency of Fresnel zone plates, which results in many variations of zone plates. One of the important variations is the phase zone plate [37,38]. In phase zone plates, the opaque zones are replaced with a material that can change the phase of the incident wave by $\lambda/2$. Hence light from all the zones constructively interferes at the focus spot. Although the transmission efficiency of the phase zone plate is 1, the focused spot size is still determined by diffraction limited.

One potential method for surpassing the diffraction limit to better focus the light for sub-diffraction nano-focusing lies in reducing the width of the open/transparent zones[20,21,39]. This approach will be the focus of the future study as described in Section 6.

4.3 Zone Plate Fabrication

Several techniques were adapted for the fabrication of the Fresnel Zone plate with the dimensions <10's μm indicated on Table 6. Although the feature sizes on the fabricated zone plate are achievable using the current photolithographic techniques, the complexity of the design and the need to prepare a mask which is both time and money consuming, poses major problems in the fabrication process [40].

The first method used in this study for the fabrication of Fresnel zone plate was Focused Ion Beam (FIB) milling. In this technique, the zone plate structure (i.e. the dark zones) was directly milled into a 300nm thick silver coating deposited by thermal evaporation using a BOC Edwards 306 system (Pressure: 10^{-6} Torr) on a quartz substrate. An SEM image of the fabricated structure is shown in Figure 26. The major problems appeared when using FIB for fabricating zone plate structures on silver thin film are (1) the

fabrication edge is not smooth because of the high energy Ga+ ion utilized in removal the Ag coating. Sometimes, the coating is entirely exfoliated during the FIB fabrication, (2) because FIB is a milling process with metallic ions, it leaves significant amount of residue (i.e., metallic ions) on the sample after the fabrication, which changes the designed optical properties of the substrate, (3) undesired under-cutting of the substrate material (quartz in this case) occurs during the milling process. As a result, the base material is not smooth as preferred in the zone plate design after the fabrication [41], (4) the maximum resolution with FIB is not as good as the state-of-art e-beam available today.

Due to the above mentioned drawbacks encountered during the FIB, e-beam lithography was explored as a possible option for the successful fabrication of Fresnel Zone plates in the second year of this study.
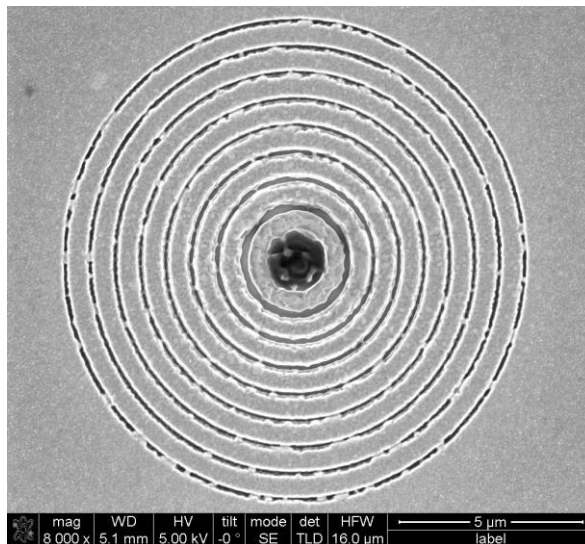

Figure 26: SEM image of zone plate fabricated using FIB milling

Electron beam lithography (or e-beam lithography) has been shown to produce line widths as small as <10nm [42]. Similar to photolithography used in micro-fabrication, e-beam lithography uses electron beam sensitive resists to generate patterns on different

substrates. There are two common ways to generate nano-patterns on substrates with e-beam lithography using positive or negative e-beam sensitive resists.

The first one, which is more direct method, is based on an etching process. Most of the fabrication processes that involve patterning on metal thin films with e-beam lithography use the etching process. In the lithography-etching process, a metal thin film is first coated on the substrate (either glass or quartz). A highly etch resistant positive e-beam resist (such as UV-5) is then spun on to the metal surface. Positive e-beam lithography is performed on the photoresist layer above the metal coating, which leaves desired patterns on the resist after exposing to e-beam and immersion in developer. The patterns on the resist are then transferred to the underlying metal thin film through reactive ion etching (RIE) of the selected region of the metal film (i.e., not protected by the patterned resist). The anisotropic nature of dry etching techniques such as RIE ensures an accurate transfer of the patterns.

Zone plate fabrication with the above mentioned technique has been done on a 100 nm thick titanium thin film coating using UV-5 as an etch resistant resist [20]. However zone plates fabricated using the direct process suffer from (1) lack of sharp edges due to high energy ions used for etching, (2) difficulty to fabricate zone plates with thick metal coatings, due to requirement of a highly etch resistant e-beam resist and (3) tendency to have exfoliation of some metals like silver, during the etching process due to the high energy ions striking on the silver coating, thereby destroying the fabricated structure.

Besides the direct etching process as described above, nano-patterns can be generated through a lift-off process. In micro-fabrication, while the etching process is used to generate patterns on metal films, lift-off is used to generate metal patterns on substrate materials such as Si or quartz. Lift-off is done by patterning on a high resolution positive resist (PMMA), followed by metal deposition on the patterned substrate after resist development. The underlying resist is then lifted off using a standard resist stripper,

leaving the metal pattern on the substrate material in the areas where the resist was completely removed in the development stage. Using multi-layers of resist combinations (such as PMMA/MMA) under cut profiles can be created and have been shown to produce very accurate lift off results [43]. Compared with direct etching, lift-off process has the following advantage in micro zone plate fabrication, namely, (1) lift-off can produce features with smooth edges if significant undercut is present in the resist layer; (2) lift-off does not suffer from metal exfoliation problems which occur in etching techniques; (3) lift-off allows flexibility in increasing the thickness of the metal film by increasing both the thickness of the resist and the etching time, to provide undercut.

However, a traditional lift-off process cannot be applied directly for fabrication of zone plates using e-beam lithography, since patterning on a metal film using the lift-off method requires a negative lift-off process. Using a positive resist in such applications requires exposure of large areas of the resist thereby consuming a lot of e-beam time and making high resolution patterning difficult in line scanning lithography techniques like e-beam lithography. Although negative e-beam resists can be used to fabricate zone-plate structures using e-beam lithography and lift-off, most of the commonly used negative resists have a poor resolution. Hydrogen silsesquioxane (HSQ), a negative resist, has been introduced recently due to its high resolution capability, minimum edge roughness, excellent etch resistance and good stability [44]. However, despite the high resolution, HSQ is difficult to lift off making is unsuitable for zone plate fabrication using a traditional lift-off technique.

To solve these issues, an indirect lift-off process was applied in this study for the fabrication of zone plate using e-beam lithography. Recently it has been shown that e-beam lithography of HSQ/PMMA bi-layers can be used for negative tone lift-off process, using HSQ as a top layer and PMMA resist as an under layer, which combines the high resolution capability of the HSQ negative resist and the good lift-off characteristic of PMMA [45]. However most of the applications using HSQ/PMMA bi-

layers focused on fabrication on silicon substrates that are conducting and well suited for charge dissipation in e-beam lithography [46,47]. Since the zone plate has to be fabricated on an insulating substrate (normally BK-7 or fused silica) an adequate conducting path has to be provided to prevent charging effects during e-beam exposure. Substrate charging causes distortions in the generated patterns, mainly due to beam deflection by the net negative charged gained by the substrate due to charge accumulation [40].

In this study, a number of variations of indirect lift-off techniques were developed to minimize charging effects while fabricating the zone plate on a quartz substrate with HSQ/PMMA negative lift-off process. A detailed description of each of these approaches, including the problems associated with each is presented in the following sections. Note that in all the conditions described, e-beam patterning was carried out with a JEOL-6460 SEM system adapted for e-beam lithography at an acceleration voltage of 30kV. The exposed HSQ was developed using MF-319 (0.23N TMAH) developer at room temperature for 60seconds, rinsed in DI water and blow dried using N_2 gas. Also the thermal evaporation of metal thin films was carried out at a pressure of 10^{-6}Torr with a deposition rate of 0.02-0.2nm/second in a BOC Edwards 306 vacuum thermal deposition system.

The first approach to prevent charging effects is to evaporate a thin film of gold, chromium or aluminum on top of the patterning resist. The presence of the thin film does not significantly scatter the incident electrons; however, acts as a charge dissipation layer during e-beam patterning. The coated metal thin film is removed with suitable wet etchant before the resist development process [40]. This idea has been successfully demonstrated for the fabrication of nano-structures on a glass substrate using ZEP520A resist with a gold thin film over-layer [48]. However, a potential issue with this technique is the compatibility between the metal and the applied resist. In this study, it was found that the available metal thin films (e.g., gold and aluminum) either showed poor adhesion with HSQ resist or the etchant used to remove the metal film reacted with the

exposed resist. In general, metal layer for charge dissipation is not a universal solution to prevent charging since it is highly selective to the type of resist and substrates used in the fabrication.

In the second technique, Indium tin oxide (ITO) coating on the substrate (i.e., glass) was used as the charge dissipation layer [49]. While the ITO coating is transparent in the visible regime, with a transmissivity of 90%, it is also acts as a conducting layer for electron discharge during e-beam lithography. Figure 27 shows a schematic of the process employed. In this study, ITO glass (from SPI supplies), a commercially available glass sample coated with 80 nm of ITO, was used as the substrate material. A HSQ/PMMA bi-layer consisting of 200 nm of PMMA (3%PMMA in MCB) and 30 nm of HSQ (2% in MIBK) was spin coated on the ITO surface. After e-beam patterning at 30 kV, the HSQ film was developed and the pattern was transferred to PMMA with RIE using O_2 plasma (pressure: 100 mT Flow rate: 20 sccm RF Frequency: 150 W) for 60 seconds. Etching of the PMMA layer for 1minute using the above mentioned RIE conditions ensured significant undercut profiles necessary for a good lift-off process [50]. A 150 nm silver thin film was deposited on the etched substrate using thermal evaporation. Lift off was carried out by immersing the sample in an ultrasonic acetone bath for 1 minute. An SEM image of the fabricated zone plates is shown in Figure 28.
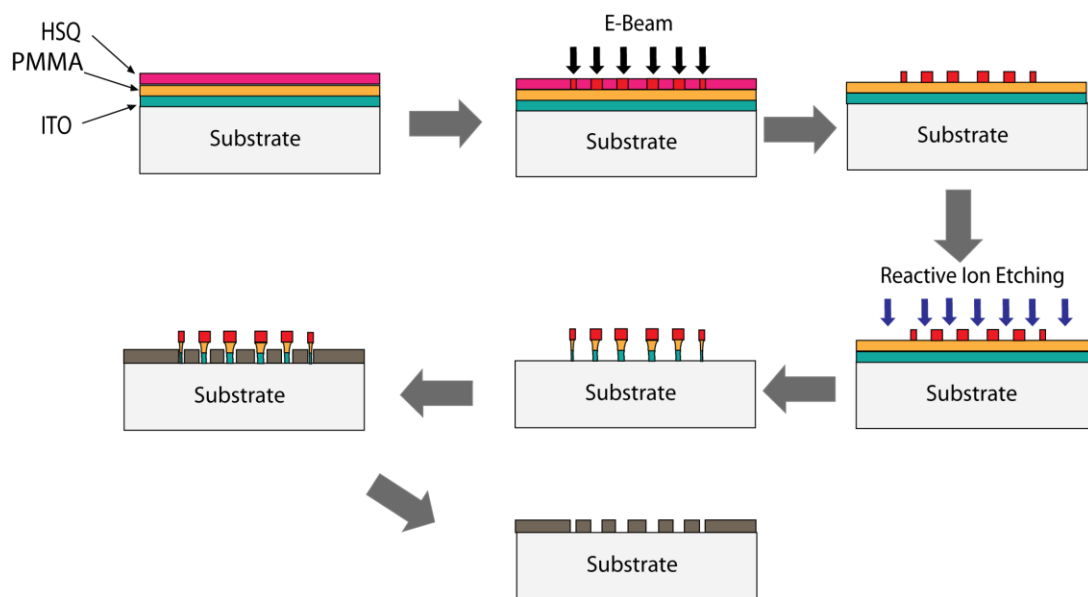
Figure 27: Schematic of fabrication process using ITO coated substrate

When this zone plate was tested for pattern generation on photoresist, it was found that, in order to completely block laser light propagation through the silver film and the dark zones of the zone plate, the silver film thickness should be >200 nm for constructing opaque enough regions in the zone plate design. In the above mentioned approach, the way to increase the silver film thickness is to increase the PMMA film thickness to >280-300 nm.
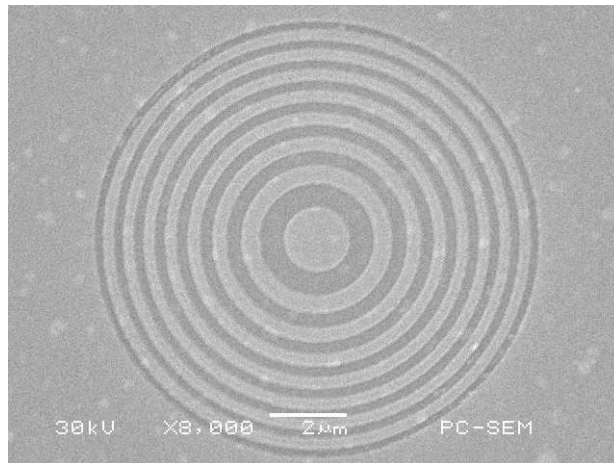
Figure 28: SEM image of zone plate fabricated with a 200nm thick PMMA layer. Thickness of silver coating ~150nm

The PMMA thickness was increased from 200 nm to 300 nm to enable the deposition of a 250nm thick silver film after etching. An optical microscope image of the fabricated structures after the RIE process is shown in Figure 29. The array of zone plates was fabricated with increasing dosage from 0.8 nC/cm to 1.8 nC/cm. It can be seen that the resist is under exposed to a dosage of 1.5 nC/cm and for the subsequent dosage values the resist is overexposed leading to a significant broadening of the features such that no ring structures can be seen.
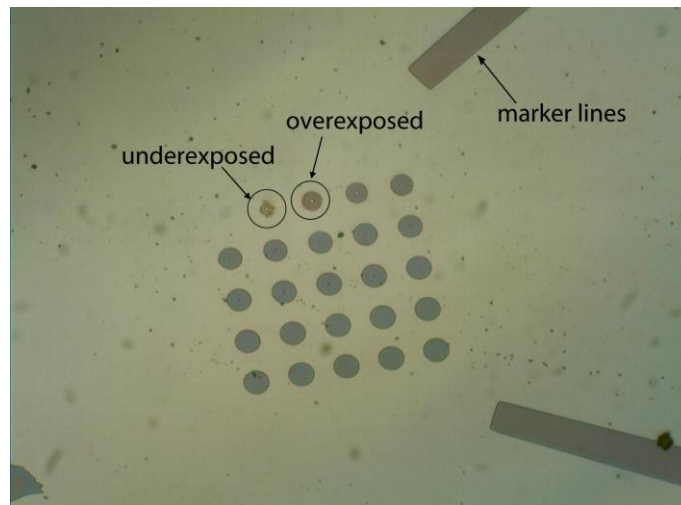
Figure 29: Optical microscope image showing the overexposed and underexposed patterns in the fabricated array after etching process when the PMMA under layer thickness was increased to 300nm

The broadening of the ring structure can be attributed to the proximity and charging effects of the e-beam resist during e-beam lithography. The proximity effect is a common phenomenon in e-beam lithography that causes pattern broadening due to increased electron back-scattering. For an accelerating voltage of 30kV the range of electrons in PMMA can be in the order of microns [40]. Hence, the increase in the PMMA thickness can significantly increase the electron backscattering. The backscattered electrons from the thicker PMMA layer can expose the negative HSQ resist, resulting in broadening of the pattern. Another possible contributing factor to the pattern broadening process is the substrate charging. Since the thickness of the conducting ITO layer used in this study is ~80nm, it may not be thick enough to conduct away all the transient high speed electrons during the lithography, especially for high accelerating voltages of 30kV, since the electrons may have sufficient energy to pass through the layer into the substrate [51]. The electrons embedded in the insulating substrate take a longer time to move to the ground, causing deflection of the incident electron beam due to the build-up of negative charge in the substrate. This can also contribute to pattern broadening. The detailed study of the proximity and charging effects during e-beam lithography is

beyond the scope of this study, and will be continued in the future work.

One way to solve this structure broadening problem is to reduce the beam accelerating voltage such that most of the incident electrons either stop in the resist or near the conducting layer. Reducing the acceleration voltage also reduces the electron range, thereby reducing proximity effect [40]. Figure 30 shows an SEM image of a zone plate fabricated with an acceleration voltage of 20kV. As it can be from the image, zones of the fabricated zone plate are visible unlike the previous case, indicating that the pattern spread due to proximity effect and substrate charging has been significantly reduced. However, the edges are not smooth, mainly due to the increased forward scattering within the HSQ layer as a result of reduction of the incident electron energy. Although a balance between these two effects can be reached to fabricate better structures by suitably varying the accelerating voltage, the process is too sensitive to resist thickness and does not provide a reliable solution for the fabrication of zone plate like nano-structures on insulating substrates.
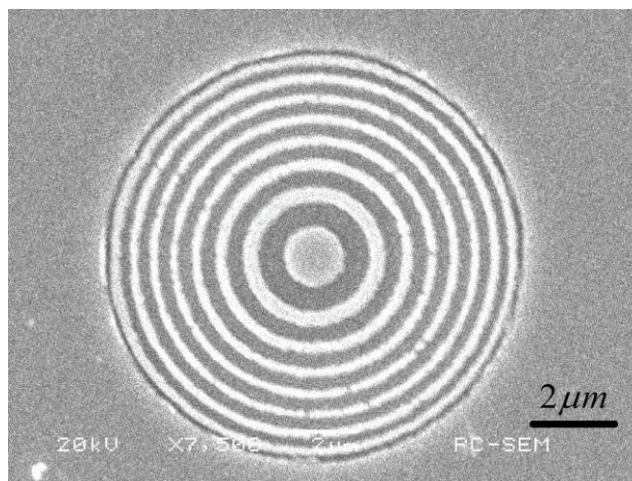

Figure 30: SEM image of zone plate fabricated with a 300nm thick PMMA under layer and an acceleration voltage of 20kV

In the final technique used for zone-plate fabrication a layer conducting polymer was

used as a charge discharge layer during e-beam patterning.

Conducting polymers have drawn significant attention for charge dissipation during e-beam lithography recently, mainly because of their high conductivity and ease of processing and compatibility with existing micro-fabrication processes (e.g., conducting polymers can be easily spin coated on to the substrate for generating a discharging layer. Also, some polymers can be easily removed with low reacting solutions) [52]. Polyaniline (PANI) is one of the preferred conducting polymers in e-beam lithography because of its environmental stability, easy synthesis from inexpensive raw materials and compatibly with most commonly used e-beam resists [53]. Conducting polyanilines have been used as removable SEM discharge layers and as dissipating layers in lithography applications that use very thick resist layers on silicon wafers [54]. Conducting polyanilines are also suitable for pattern transfer processes as they can be removed by RIE using O2 plasma unlike most of the metal discharge layers [52]. However, PANI has not been tested as a charge dissipation layer when fabricating nanostructures on insulating substrate materials like glass or quartz.

In this final attempt, the HSQ/PMMA bi-layer negative lift off process was used for the zone plate fabrication. A layer of conducting polyaniline was sandwiched between two PMMA layers as shown in Figure 31. Since the PMMA layer above the conducting polyaniline is only 110nm thick, the overexposure problem that occurred in the previous technique is prevented. Note that both polyaniline and PMMA can be etched with an O2 RIE process and dissolved using the same resist stripper (NMP). As a result, the entire PMMA/PANI/PMMA tri-layer can be used as the pattern transfer layer for the lift-off process. This advantage is very difficult to achieve with the ITO-glass technique where the entire fabrication process takes place over the ITO coating. The reason for the presence of a PMMA layer above the PANI is due to the compatibility problem between HSQ and PANI which was identified after several tests. Hence, by adequately adjusting the PANI and PMMA thickness, it is possible to generate patterns even on 500nm thick

metal films without any problems of overexposure due to a thick underlying resist.

A detailed description of the fabrication procedure adapted when using PANI as the discharge layer is as follows:

1. A 50nm thick layer of PMMA (2% in SBC) was spin-coated on a cleaned quartz plate at a spin speed of 400rpm. The PMMA coated substrate was baked at 120^0C for 2 minutes.

2. Over this PMMA layer, a 120nm thick layer of PANI (20% in NMP) was spin coated at a speed of 200rpm. A detailed description of the conversion of PANI powder (emeraldine base) into a spin coatable form is provided in Appendex--. The sample was then baked on a hot plate at 180^oC for 15 minutes.

3. PANI, in its base form is non-conducting and has to be doped with aqueous protonic acids like HCl or H2SO4. The PMMA/PANI coated sample was immersed in a solution of 0.1N HCl for 6hrs to give conductivity of the order of 1S/cm2 (REF). The sample was then washed in DI water and baked on a hot plate at 120^oC.

4. Following this process, the HSQ/PMMA bilayer consisting of 150nm of PMMA and 30nm of HSQ was coated over the PANI layer for e-beam patterning. Note that the available thickness to facilitate a lift off process is now the total thickness of the PMMA/PANI/PMMA tri-layer which is 350nm. This thickness is sufficient to lift off even a 320nm thick metal film if significant under cut is provided.

5. E-beam lithography was performed at 30kV over the HSQ and the patterned sample was developed. The pattern was then transferred to the quartz substrate using reactive ion etching (RIE) in O2 plasma. Since the total thickness of the PMMA/PANI/PMMA layers used in this application was only 280nm, RIE was carried out for 90seconds (pressure: 100mTorr Flow rate: 20sccm RF Frequency: 150W) to obtain undercut profiles.

6. A 230nm thick silver thin film coating was deposited on the etched substrate by thermal evaporation process and the lift off process was carried by immersing the sample in NMP for 1 minute.

An SEM image of the zone plate fabricated using this process is shown in Figure 32. Although an image showing a direct view of the undercut profiles was not obtained in this study, the sharp edges obtained after the lift off process indicate that the undercut was sufficient to enable a good lift-off.
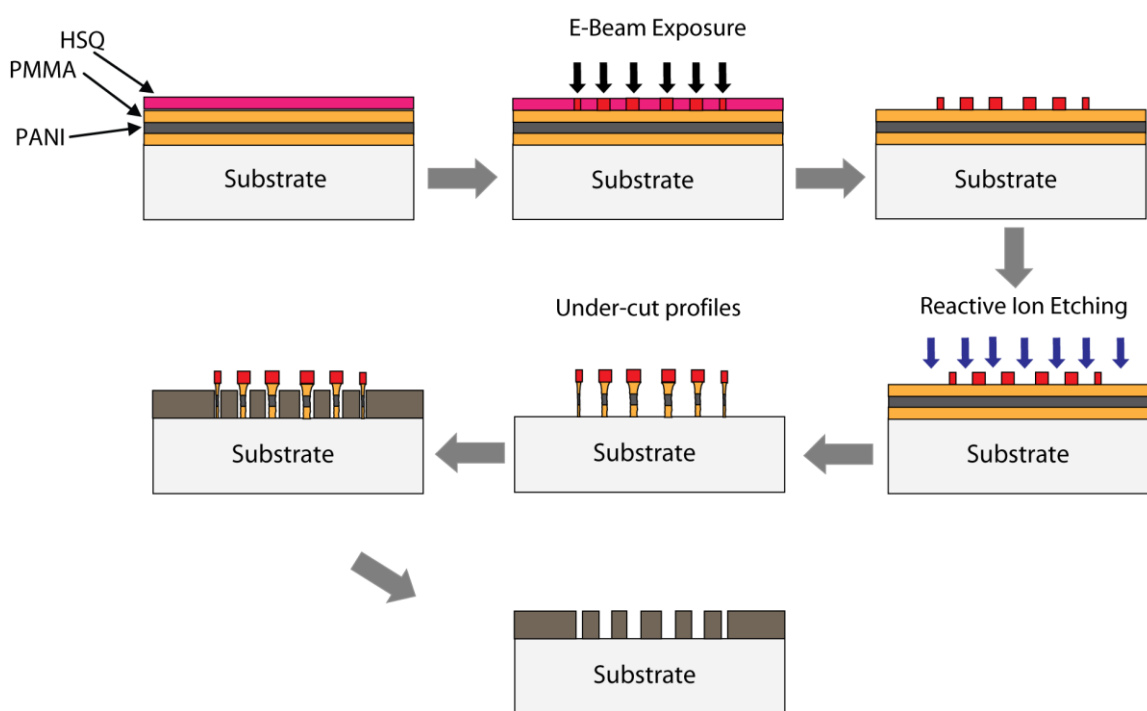
Figure 31: Schematic of fabrication process when polyaniline was used as a conducting layer for charge dissipation

The focusing efficiency of the fabricated zone plate with 409nm laser light was tested by pattern generation on a UV sensitive photo-resist. A detailed description of the

experimental setup used and the patterns generated on the photo-resist will be provided in the following sections.
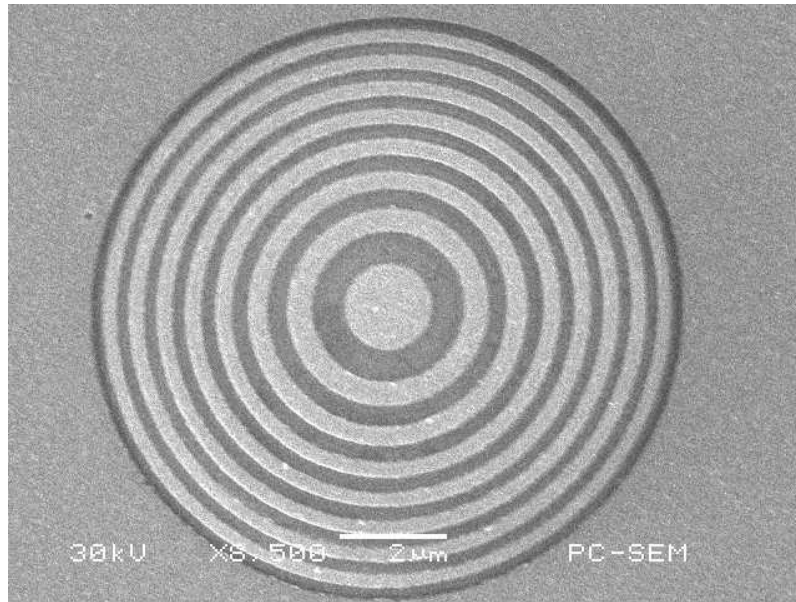
Figure 32: Final fabricated zone plate structure

5. NANO-LITHOGRAPHY WITH MICRO ZONE PLATE – EXPERIMENT

5.1 Experimental Setup
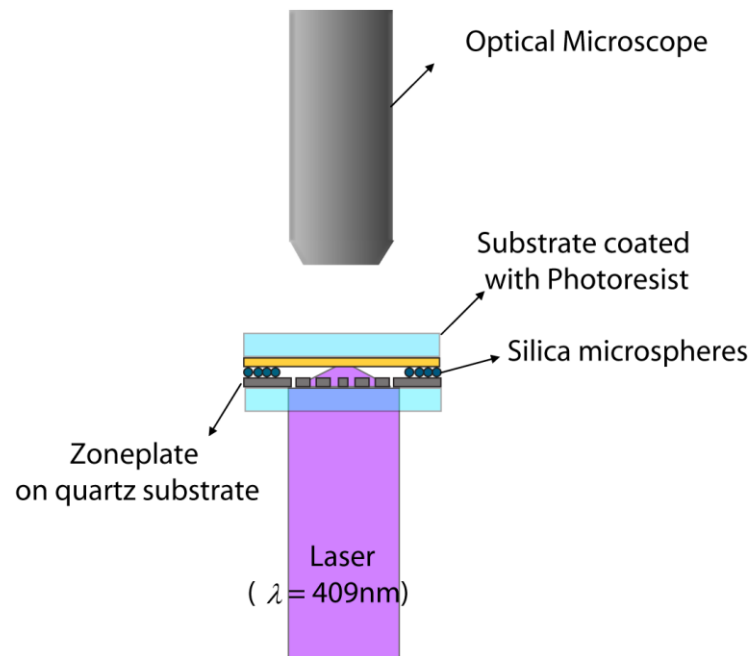
Figure 33: Schematic of experimental setup

A schematic showing the setup used to test the focusing of the zone plate is in Figure 33. The silver thin film coating on which the zone plate structure was fabricated and was dispersed with 3micron diameter SiO2 spheres. The diameter of the spheres was chosen to be equal to the design focal length of the traditional zone plate in order to maintain the separation distance between the zone plate and the target surface. The spheres were first ultrasonically dispersed in ethanol solution for about 5mins. Less than 0.5ml of the solution was then dropped around the edges of the zone plate sample with a pipette while the sample was maintained at a temperature of about 40°C. Note that the zone plate

structure was fabricated on the center of the quartz plate (with suitable marker lines for identification) and the solution containing micro-spheres was dropped around the edges making sure that it does not spread to the center region. Direct vaporization of the ethanol solution results in the formation of multi-layers of microspheres especially along the edges of the 'solution dropped region'. In order to obtain a uniform monolayer of microspheres, a modified convective assembly process was used to deposit the spheres [55,56]. In this technique a cleaned quartz plate was gradually placed over the droplet deposited onto the zone plate sample, thereby entrapping it by capillarity effect. The quartz plate was then gradually moved making sure that solvent (ethanol) vaporizes when the region was exposed. This is depicted in Figure 34. As the exposed ethanol vaporizes, it leaves behind a uniform monolayer of silicon microspheres on the surface of the sample. Care was taken to ensure that excess pressure was not applied over the quartz plate in order to prevent scratching of the silver coating. This process was repeated on all the four edges of the quartz plate. Figure 35 shows an image of a uniformly dispersed monolayer of 3 micron spheres on the silver coating as viewed under an optical microscope. A quartz plate was then spin coated with 300nm thick film of S-1805 photoresist coating and placed on top of the microsphere coated zone plate sample with the coating side facing down. The 3 micron spheres, acting as spacer, ensures that the photoresist coating is placed at a distance of 3microns from the zone plate, which corresponds to the design focal length of the zone plate.
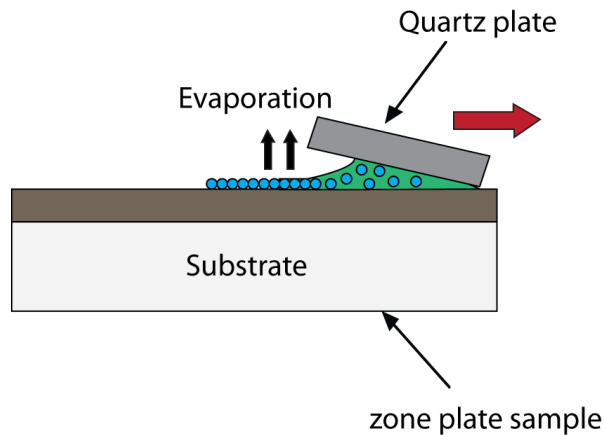
Figure 34: Schematic showing the method used to disperse a monolayer of microspheres
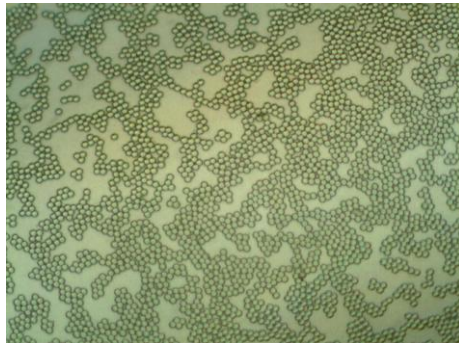
Figure 35: Optical microscope image of microspheres dispersed on the zone plate sample

A pulsed nanosecond Nd-YAG laser (OPOTEK Vibrant 355 II) was utilized as the light source. The pulse width of the laser was ~4ns with a repetition rate 10Hz and energy fluctuation <10%. The wavelength was adjusted to be λ=409 nm through an optical parametric oscillator (OPO). The nanosecond laser was externally triggered by a delay generator (SRS DG535) with a repetition rate of 10Hz. The nanosecond laser light is conducted to the zone plate using a system of mirrors and a convex lens. An optical microscope located above the zone plate was used to position the zone plate in the path of the laser beam and expose the photoresist coating at the desired labeled position.

The photoresist was then developed using MF-319 developer and the generated pattern on the photoresist is scanned using an AFM.

5.2   Results and Discussion

Figure 36 shows a surface topographical image (and pattern profile) of the pattern generated after 50 laser pulses on the photoresist. The pattern diameter was ~800nm and FWHM is about 400nm. The slight difference between the pattern diameter values predicted by the scalar diffraction theory and the experiment could be due to differences in the separation distance between the sample and the zone plate. Note that although a monolayer of *3μm* diameter spheres was dispersed on the zone plate sample to maintain the separation equal to the design focal length, an optical microscope image of the patterned resist showed significant imprint of the hard spheres into the soft resist layer. Since the thickness of the resist used was about 200nm, the real separation distance between the resist surface and the zone plate was less than 3microns.
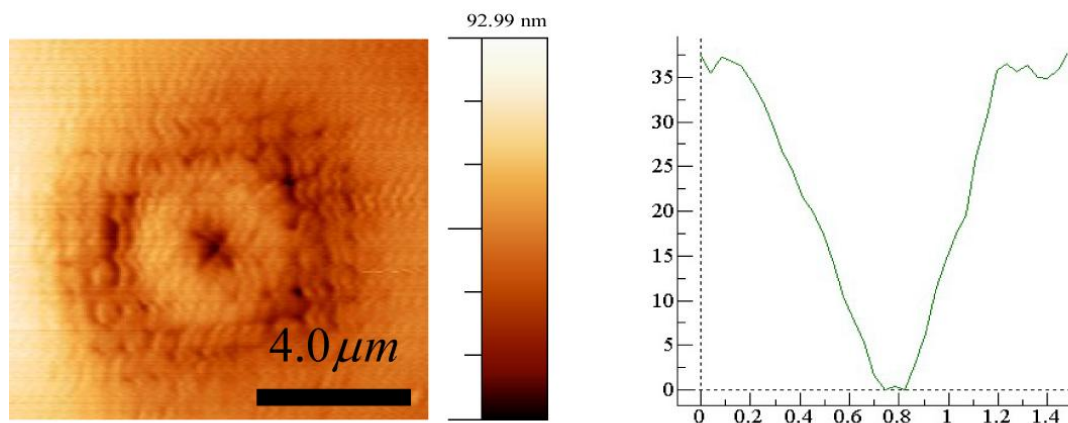

Figure 36: Surface topography image of pattern generated on photoresist after 50 laser pulses

To understand the contribution of the number of laser pulses along with the associated increment in the light dosage on the generated patterns, four different number of laser pulses, namely, 30, 50 100 and 150 laser pulse, were examined in this study. Figure 37

shows a surface topographical image of the patterns generated on the photoresist (after development) scanned with an AFM system. The images correspond to 30, 50, 100 and 150 laser pulses with an input energy of *0.68J/cm²*. The pattern depth and diameter increases with the increase in the number of laser pulses. Also, from the AFM images it can be seen that an annular affected region of about *3μm* diameter, surrounds the central spot generated at the focus point. Comparing the pattern with the intensity distribution obtained from numerically solving the Rayleigh-Sommerfeld diffraction integral, the annular affected region corresponds to the high intensity side-lobes that appear in the intensity distribution (Figure 25) at a distance of *1.5μm* from the focus spot. Since the intensity at the focus spot is ~10 times more than that at the side lobes, the pattern depth at the focus spot is larger than the annular region.
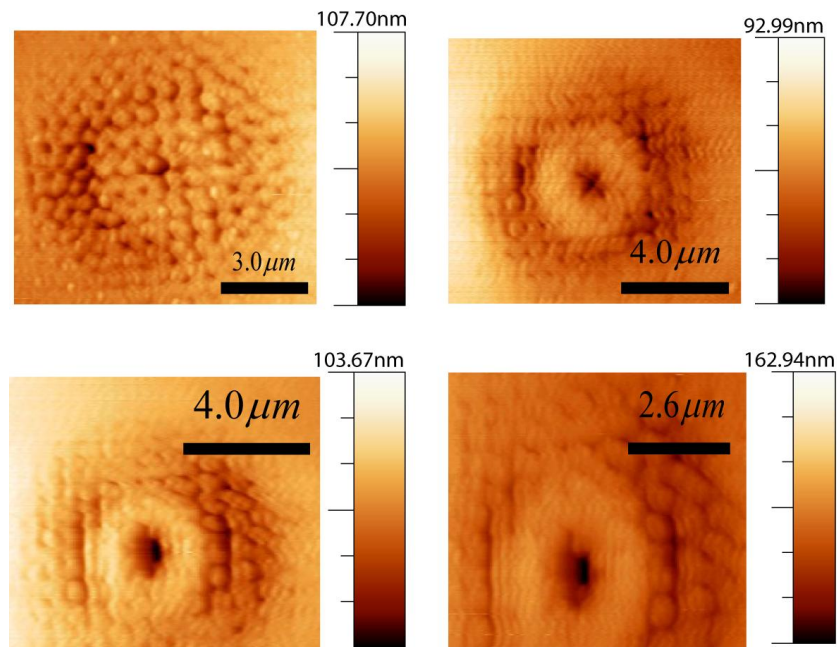
Figure 37: Patterns generated on S-1805 photoresist after 30, 50, 100 and 150 laser pulses

Reducing the intensity at the side lobes can eliminate the occurrence of the annular ring structure in the photoresist pattern. The side lobes occur at a distance of *1.5μm* from the centerline of the zone plate. The effect of increase in the number of zones of the zone

plate on the side lobe intensity was analyzed. The Rayleigh-Sommerfeld integral was solved for a zone plate with four extra zones (a total of 12) to determine the intensity distribution. The intensity at the peak increased to ~13 times the side lobe intensity but the FWHM remained the same (Figure 38). Although the zone width of the Fresnel zone plate converges to a value equal to half the wavelength of the incident light, increasing the number of outer zones can significantly reduce the occurrence of annular structures during the pattern generation process, which will be demonstrated experimentally in the future study.
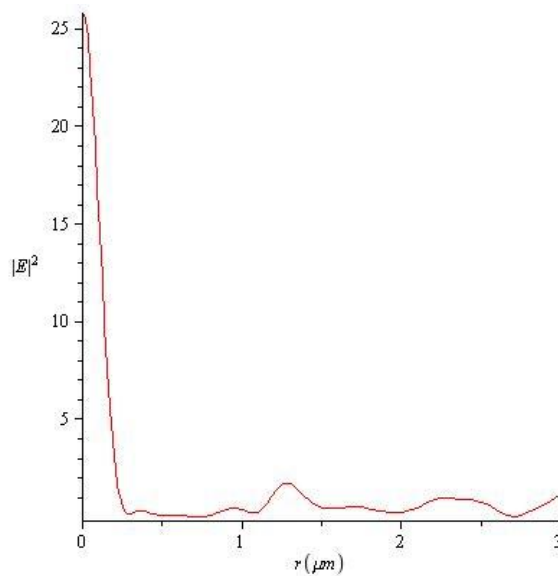
Figure 38: Intensity distribution showing reduced side lobes when the number of zones was increased to twelve

5.3   Summary

A traditional Fresnel zone plate with a focus length of 3μm for an incident wavelength of 409nm was fabricated on a 300nm thick silver thin film coating with a novel lift-off process in e-beam lithography. The novel process involved using a HSQ/PMMA bi-layer in a negative tone lift-off process with a layer of conducting polyaniline for charge dissipation. HSQ was used as the high resolution negative resist for e-beam patterning

and the PMMA under-layer was used to enable a HSQ lift-off process. The conducting polymer, polyaniline (PANI), was introduced to minimize the charging and proximity effects in the e-beam fabrication on insulating substrates. Since the entire e-beam lithography and charge dissipation process takes place above the PANI layer, the thickness of the underlying PMMA can be varied depending on the desired metal coating thickness required. The fabrication procedure developed in this study thus provides a standard route for fabrication of Fresnel zone plates and future fabrication of plasmonic sub-diffraction limit zone plate structures.

It was demonstrated that the fabricated zone plate could focus light to a spot with a focus length of 3μm. Patterns of ~800nm diameter were generated on a photoresist (FWHM ~ 400nm) with a parallel plate experimental setup allowing the adjustment of separation distances with solid microspheres as spacers. The scalar diffraction theory was used to numerically predict the intensity distribution at the focus spot. The annular ring structure on the pattern generated on the photoresist was shown to be the result of the side lobes that occurred in the numerically calculated intensity distribution. The intensity at the side lobes could be significantly reduced by increasing the number of outer zones in the fabricated zone plate. Patterns generated on the photoresist, in this study, were larger than the theoretical values predicated from scalar diffraction theory as a result of variations in the separation distance between the zone plate and the sample (due to imprint of spheres on the photoresist). Nevertheless, the parallel plate experimental setup provides an ideal platform for preliminary testing of Fresnel zone plates and sub-diffraction limit plasmonic zone plate devices.

6. CONCLUSIONS AND FUTURE WORK

In this master's thesis, nano-patterning was carried out with two different nano-optic devices - NSOM and the micro zone plate. In NSOM studies, intense sub-diffraction limit light emission was achieved with a combination of apertured NSOM probes and pulsed ns/fs pulsed lasers. In this portion of study, nano-patterns have been successfully generated on different semiconducting and metallic targets. It was observed in this study that the laser pulse duration, number of laser pulses and laser energy have strong contributions on the pattern generation process. When femtosecond laser was coupled with NSOM probes, sharper and cleaner sub-diffraction limit patterns could be generated on different targets. The pattern generation threshold with femtosecond lasers was <1 nJ. Also, femtosecond laser caused little (i.e., not observable) thermal damage to the NSOM probes even under high input laser energies (>3nJ). When ns laser was applied as the light source, much higher light intensity (>2 nJ) was required for generating nano-patterns on the similar targets compared with fs laser. In addition, melting of the metal coating in the NSOM tip was observed when the input ns laser energy >2.2-2.5nJ. Three different mechanisms were identified as the dominant processes for pattern generation under different conditions, namely nano-scale laser ablation, nano-scale thermal oxidation and nano-scale melting/recrystallization of the targets. The importance of each mechanism on nano-pattern generation is a function of optical and material conditions in NSOM experiments as discussed in Section 3.

The experiments with a combination of nanosecond laser and NSOM probes showed that nano-pattern generation on different targets under high laser fluence, without causing any thermal damage to the NSOM probe, is very challenging (mainly because of the slight difference between the damage threshold and pattern generation threshold). Femtosecond laser provides much more desired results in terms of precision of the generated nano-patterns along with a big range of applicable laser energies with no

observable damage of the NSOM probes during operation. However, the high costs of femtosecond laser systems may prohibit the combination of fs laser with NSOM probes for nano-pattern generation in industrial applications. One way to perform high energy direct nano-patterning using NSOM and nanosecond lasers is to modify the design of NSOM tips to withstand high nanosecond laser fluence based on the knowledge of how thermally induced damages occur . The experimental methods adapted in this study provided an indirect approach to understanding mechanisms of energy transport with a combination of NSOM system and pulsed laser sources. A better physical picture of the origin of the damage and the laser induced heating processes in the NSOM tip can be obtained with rigorous numerical simulations considering both optical and thermal energy transport in the NSOM tip during pattern generation processes. The temperature distribution in NSOM tips, obtained from simulations and non-contact temperature measurements, can be used to improve the design of the NSOM probe (e.g., the tapering angle, the constructing material, the shape of the aperture and the operating light conditions) to withstand higher input laser energies.

Another solution to high energy direct nano-patterning would be to develop nano-optic devices which do not rely on near field effects and can also provide higher energy throughput during operation. The second half of this study thus focused on developing a plasmonic optic device based on Fresnel zone plate, capable of sub-diffraction limit light focusing. As a preliminary study, a traditional Fresnel zone plate was fabricated with a novel lift-off process in e-beam lithography developed in this master study. The focusing of the fabricated zone plate was tested by pattern generation on photoresist with a parallel plate experimental setup allowing the adjustment of separation distances with solid microspheres as spacers. The smallest pattern size generated was close to the diffraction limit as designed before the fabrication. Although this thesis covers only the preliminary studies involving diffraction limited traditional Fresnel zone plates, the fabrication technique developed during the course of this study will be used as a standard technique for fabrication of both Fresnel zone plates and plasmonic sub-

diffraction limit zone plate devices. It is noted that plasmonic devices based on Fresnel zone plates are still under study in current literature unlike commercialized NSOM systems. Plasmonic zone plates will be more preferred in the future study because a much higher light transport efficiency can be achieved (>0.1). Also, the plasmonic zone plates can provide a longer working distance compared with traditional NSOM system.

In the future studies, the following three topics can be emphasized for achieving a better sub-diffraction limit pattern with a combination of plasmonic zone plates and NSOM techniques:

- A thorough diffraction analysis and electrodynamics/thermal simulations to describing the light focusing limit along with the thermal limit of plasmonic zone plates.
- An integrated experimental and theoretical analysis of the performances of plasmonic zone plates with different designs and optical conditions.
- A combination of plasmonic zone plate with scanning optical probes systems to achieve sub-diffraction limit scanning type nano-patterning/nanoscale direct fabrication.

REFERENCES

[1]   D. Bäuerle, *Laser Processing and Chemistry*, 2nd ed. (Springer, Berlin; New York, 1996).

[2]   I. W. Boyd, *Laser Processing of Thin Films and Microstructures: Oxidation, Deposition, and Etching of Insulators* (Springer-Verlag, Berlin ; New York, 1987).

[3]   W. Demtröder, *Laser Spectroscopy*, 2d. enl. ed. (Springer-Verlag, Berlin, New York,, 1973).

[4]   C. R. Phipps, and B. S. Lukianchuk, *Laser Ablation and Its Applications* (Springer, New York, 2007).

[5]   C. P. Grigoropoulos, *Transport In Laser Microfabrication: Fundamentals and Applications* (Cambridge University Press, Cambridge, 2009).

[6]   L. Novotny, and B. Hecht, *Principles of Nano-Optics,* (Cambridge University Press, Cambridge, 2006).

[7]   E. Betzig, and J. K. Trautman, Science **257,** 189-195 (1992).

[8]   E. Betzig, J. K. Trautman, T. D. Harris, J. S. Weiner, and R. L. Kostelak, Science **251,** 1468-1470 (1991).

[9]   N. Hayazawa, Y. Inouye, Z. Sekkat, and S. Kawata, Chemical Physics Letters **335,** 369-374 (2001).

[10]   N. Hayazawa, Y. Inouye, Z. Sekkat, and S. Kawata, Journal of Chemical Physics **117,** 1296-1301 (2002).

[11]   M. K. Herndon, R. T. Collins, R. E. Hollingsworth, P. R. Larson, and M. B. Johnson, Applied Physics Letters **74,** 141-143 (1999).

[12]   S. B. Wen, R. Greif, and R. E. Russo, Applied Physics Letters **91,** 251113 (2007).

[13]   V. Zorba, X. L. Mao, and R. E. Russo, Applied Physics Letters **95,** 041110 (2009).

14 D. J. D. Carter, D. Gil, R. Menon, M. K. Mondol, H. I. Smith, and E. H. Anderson, Journal of Vacuum Science & Technology B **17,** 3449-3452 (1999).

15 D. J. D. Carter, D. Gil, R. Menon, I. J. Djomehri, and H. I. Smith, Emerging Lithographic Technologies Iii, Pts 1 and 2 **3676,** 324-332864 (1999).

16 I. J. Djomehri, T. A. Savas, and H. I. Smith, Journal of Vacuum Science & Technology B **16,** 3426-3429 (1998).

17 D. Chao, A. Patel, T. Barwicz, H. I. Smith, and R. Menon, Journal of Vacuum Science & Technology B **23,** 2657-2661 (2005).

18 C. Genet, and T. W. Ebbesen, Nature **445,** 39-46 (2007).

19 H. J. Lezec, A. Degiron, E. Devaux, R. A. Linke, L. Martin-Moreno, F. J. Garcia-Vidal, and T. W. Ebbesen, Science **297,** 820-822 (2002).

20 S. Seo, H. C. Kim, H. Ko, and M. Cheng, Journal of Vacuum Science & Technology B **25,** 2271-2276 (2007).

21 H. C. Kim, H. Ko, and M. Cheng, Journal of Vacuum Science & Technology B **26,** 2197-2203 (2008).

22 E. Hecht, *Optics*, 4th ed. (Addison-Wesley, Reading, Mass., 2002).

23 C. Yeh, *The Essence of Dielectric Waveguides* (Springer, New York, 2008).

24 S. A. Campbell, *The Science and Engineering of Microelectronic Fabrication*, 2nd ed. (Oxford University Press, New York, 2001).

25 S. B. Wen, Journal of Applied Physics (submitting).

26 L. Zhu, G. Gamez, T. A. Schmitz, F. Krumeich, and R. Zenobi, Analytical and Bioanalytical Chemistry **396,** 163-172 (2010).

27 W. G. Roeterdink, L. B. F. Juurlink, O. P. H. Vaughan, J. D. Diez, M. Bonn, and A. W. Kleyn, Applied Physics Letters **82,** 4190-4192 (2003).

28 J. P. Girardeau-Montaut, and C. Girardeau-Montaut, Physical Review B **51,** 13560 (1995).

29 V. Sundaram, and S. B. Wen, ASME **HT2009-88225** (2009).

30 N. Birks, G. H. Meier, and F. S. Pettit, *Introduction to the High Temperature Oxidation of Metals,* (Cambridge University Press, Cambridge, 2006).

31   Z. A. Weinberg, Applied Physics Letters **39,** 421-422 (1981).

32   T. R. Shiu, C. P. Grigoropoulos, D. G. Cahill, and R. Greif, Journal of Applied Physics **86,** 1311-1316 (1999).

33   M. Ohmukai, Y. Takigawa, and K. Kurosawa, Applied Surface Science **137,** 78-82 (1999).

34   D. C. O'Shea and Society of Photo-optical Instrumentation Engineers., *Diffractive Optics: Design, Fabrication, and Test* (SPIE Press, Bellingham, WA, 2004).

35   D. Hsu, J. Chen, Y. Sheng, Society of Photo-optical Instrumentation Engineers., *Holography, Diffractive Optics, and Applications: 15-17 October, 2002, Shanghai, China* (SPIE, Bellingham, Washington, 2002).

36   J. W. Goodman, *Introduction to Fourier Optics*, 3rd ed. (Roberts & Co., Englewood, CO, 2005).

37   O. Mendoza-Yero, M. Fernandez-Alonso, G. Minguez-Vega, J. Lancis, V. Climent, and J. A. Monsoriu, Journal of the Optical Society of America a-Optics Image Science and Vision **26,** 1161-1166 (2009).

38   I. N. Ross, D. A. Pepler, and C. N. Danson, Optics Communications **116,** 55-61 (1995).

39   H. Ko, H. C. Kim, and M. Cheng, Journal of Vacuum Science & Technology B **26,** 2188-2191 (2008).

40   P. Rai-Choudhury, *Handbook of Microlithography, Micromachining, and Microfabrication* (SPIE Optical Engineering Press; Institution of Electrical Engineers, Bellingham, Wash., USALondon, UK, 1997).

41   Y. Q. Fu, R. G. Mote, Q. Wang, and W. Zhou, Journal of Modern Optics **56,** 1550-1556 (2009).

42   A. Kent, J. G. Williams, and R. Kent, *Encyclopedia of Microcomputers* (M. Dekker, New York, 1988).

43   A. L. Bogdanov, and E. K. Andersson, Electron-Beam, X-Ray, and Ion-Beam Submicrometer Lithographies for Manufacturing **1465,** 324-329340 (1991).

44   M. Peuker, M. H. Lim, H. I. Smith, R. Morton, A. K. van Langen-Suurling, J. Romijn, E. W. J. M. van der Drift, and F. C. M. J. M. van Delft, Microelectronic Engineering **61-2,** 803-809 (2002).

45   H. F. Yang, A. Z. Jin, Q. Luo, J. J. Li, C. Z. Gu, and Z. Cui, Microelectronic Engineering **85,** 814-817 (2008).

46   J. R. Tao, Y. F. Chen, X. Z. Zhao, A. Malik, and Z. Cui, Microelectronic Engineering **78-79,** 665-669 (2005).

47   L. Magdenko, F. Gaucher, A. Aassime, M. Vanwolleghem, P. Lecoeur, and B. Dagens, Microelectronic Engineering **86,** 2251-2254 (2009).

48   H. F. Yang, L. Fan, A. Z. Jin, Q. Luo, C. Z. Gu, and Z. Cui, 2006 1st IEEE International Conference on Nano/Micro Engineered and Molecular Systems, China, 391-3941549 (2006).

49   M. F. G. Klein, H. Hein, P. J. Jakobs, S. Linden, N. Meinzer, M. Wegener, V. Saile, and M. Kohl, Microelectronic Engineering **86,** 1078-1080 (2009).

50   J. X. Liang, F. Kohsaka, T. Matsuo, X. F. Li, and T. Ueda, Microelectronic Engineering **85,** 1000-1003 (2008).

51   S. Tanuma, C. J. Powell and D. R. Penn, Surf Interface Anal **21** (3), 165-176 (1994).

52   M. Angelopoulos, IBM Journal of Research and Development **45,** 57-75 (2001).

53   M. Angelopoulos, J. M. Shaw, K. L. Lee, W. S. Huang, M. A. Lecorre, and M. Tissier, Polymer Engineering and Science **32,** 1535-1540 (1992).

54   M. Angelopoulos, J. M. Shaw, M. A. Lecorre, and M. Tissier, Microelectronic Engineering **13,** 515-518 (1991).

55   B. G. Prevo, and O. D. Velev, Langmuir **20,** 2099-2107 (2004).

56   Y. Wang, L. Chen, H. Yang, Q. Guo, W. Zhou, and M. Tao, Solar Energy Materials and Solar Cells **93,** 85-91 (2009).

APPENDIX A

Property Tables

Table 7: Optical and thermal properties for silicon and germanium

	Boiling Temperature (K)	Heat of Evaporation (KJ/mol)	Reflectance (%)	Absorption coefficient (cm^{-1})	Conductivity $(W \cdot m^{-1} \cdot K^{-1})$ At 300K	Thermal diffusion length (cm) in 4 ns
Silicon	3538	369	42.72	0.964×10^5	149	6×10^{-6}
Germanium	3106	334	45	6.66×10^5	60.2	4×10^{-6}

Table 8: Optical and thermal properties of copper, silver and chromium

	Boiling Temperature (K)	Heat of Evaporation (KJ/mol)	Reflectance (%)	Absorption coefficient (cm^{-1})
Copper (film thickness 250nm)	2835	300.4	3.7	$\sim 6.86 \times 10^5$
Silver (film thickness 300nm)	2435	250.58	82.1	$\sim 6.14 \times 10^5$
Chromium (film thickness 300nm)	2944	339.5	4.3	$\sim 1.13 \times 10^6$

APPENDIX B

Standard Procedure for Photolithography using Zone plate

Laser Wavelength Range: 350nm-450nm

Photoresist Used: Shipley 1800 Series (For a very thin film ~500nm use S-1805 resist)

Steps

- Coat a 500nm thick layer of S-1805 photoresist on to a cleaned quartz plate (For sample cleaning refer the "Sample Cleaning" instructions)
- This can be done by spin coating at a speed of 5000rpm for 60s
- Soft bake the resist on a hot plate at 120°C for 1min.
- Cover the resist with Al foil to ensure it is not exposed
- The entire experiment should be conducted using a red light source
- To develop the resist use MF-319 developer
- Immerse the sample into a 2:1 mixture of MF-319 to DI water for a period of 30-40 seconds
- Wash the developed sample in a DI water bath (to prevent mechanical forces from removing the resist coating do not spray water directly on the developed coating)
- To dry the sample used compressed air and hard bake on a hot plate for about 1min at 120°C

Standard procedure for preparing spin-coatable PANI

- Polyaniline (PANI) can be purchased in the emeraldine base form, from Sigma Aldrich (the molecular weight of PANI used in this study was 20,000).

- The solvent used for polyaniline in this study is 1-Methyl-2-pyrrolidinone, commercially available as NMP.

- 8% of polyaniline by weight is dissolved in NMP and the solution is mixed in an ultrasonic bath for 1hr.

- To remove the un-dissolved PANI particles the mixed solution is filtered using a 0.2µm syringe filter.

- The filtered solution can be directly spin coated to the desired thickness on to a substrate.

- Note that although the coating thickness of polyaniline can be increased by increasing the molecular weight of the emeraldine base (eg. 50,000), PANI has a tendency to gel when the solution is saturated and forms a solid mass that cannot be used.

VITA

Name:　　　　Vijay Meenashi Sundaram

Address:　　　Texas A&M University
　　　　　　　　Department of Mechanical Engineering
　　　　　　　　3123 TAMU
　　　　　　　　College Station TX 77843

E-mail Address: mvijay5186@yahoo.co.in

Education:　　B.Tech., Mechanical Engineering, National Institute of Technology, Trichy, India, 2008
　　　　　　　　M.S., Mechanical Engineering Texas A&M University, College Station Texas, 2010